Computers and Fluids 285 (2024) 106450

Contents lists available at ScienceDirect

Computers and Fluids

journal homepage: www.elsevier.com/locate/compfluid

Error assessment of reconstructed 3D Digital Replica Models: From Computed Tomography data to pore-scale simulations

Abdelkader Hammouti [a,b,*], Fatna Oukaili [c], Damien Pham Van Bang [a,b]

[a] INRS-ETE, Université du Québec, 490, Rue de la Couronne, Québec, G1K 9A9, QC, Canada
[b] École de technologie supérieure, 1100, Notre-Dame Ouest, Montréal, H3C 1K3, QC, Canada
[c] EDF R&D, Laboratoire National d'Hydraulique et Environnemental (LNHE), Chatou, 78400, France

ARTICLE INFO

Keywords:
Direct numerical simulation
Navier–Stokes equations
Solution accuracy
Digital rock physics
CT scan

ABSTRACT

The application of flow simulations on porous media, reconstructed through Computerized Tomography (CT) scans, has emerged as a prevalent methodology for the computation of rock permeability. However, constructing a proper 3D model of a rock sample is a real challenge, mainly due to the lack of a unified procedure. Indeed, to ensure precise outcomes, specific prerequisites must be fulfilled. This paper proposes a methodology to assess the convergence and accuracy of computed solutions from CT data to pore-scale simulations. Starting from 3D volume data obtained by X-ray CT, we develop a workflow to investigate the effects of the reconstructed shape on the permeability of a granular porous medium composed of glass beads. Indeed, the choices of CT scan resolution and digital rock discretization can compromise the quality and computational cost of numerical results. Especially in configurations of porous media with high solid volume fractions and very narrow porous spaces, as observed in solid/solid contact zones, which can be either under or over-resolved depending on the numerical tools used. Highly resolved Direct Numerical Simulations (DNS) are conducted to solve incompressible Navier–Stokes equations through porous media. Body-fitted meshes are employed to resolve irregular shapes accurately, ensuring precise results even with coarser meshes. The methodology is validated with challenging simulations of flows through simple cubic close packing of particles, incorporating various geometric surface modeling techniques. A convergence of the results with respect to grid resolution is obtained for low- to moderate-Reynolds-number flows. The numerical results indicate that permeability calculation strongly depends on surface processing. Finally, we apply these recommendations to construct accurate digital replica models generated from CT data of our assembly of randomly arranged glass beads in a tube. The study of the pressure drop convergence demonstrates an excellent agreement with the empirical correlation.

1. Introduction

In a few decades, the study of multiphase transport processes in porous media has acquired considerable attention, particularly in Digital Rock Physics (DRP). In geothermal energy, CO_2 sequestration, and oil and gas projects, utilizing digital replicas becomes crucial for modeling fluid flows across scales, providing a fine-scale understanding of rock properties. This innovative approach builds on the coupling between Computational Fluid Dynamics (CFD) software and the application of non-destructive techniques, such as X-ray Computed Tomography (CT) [1,2], thus offering the advantage of conducting various numerical experiments on the same sample.

Thereby, authors [3,4] utilize DRP to evaluate the porosity and the permeability of core samples under different configurations. A question that remains open is understanding and evaluating the impact of the reconstructed 3D digital model's quality on determining geomaterials' geometrical and physical properties [5,6]. Indeed, DRP couples the outcomes of digital image processing with pore-scale simulations. Consequently, the final model encompasses the uncertainties inherent in each process involved in the workflow. The absence of standard procedures poses challenges in accurately assessing porosity and permeability, making it difficult to distinguish between errors in data acquisition, geometrical modeling, and numerical modeling. Working with rock samples adds another difficulty because benchmarking with an analytical solution is impossible.

The detection of measurement errors is continuously enhanced to assess geometrical characteristics [7]. Depending on the CT instruments, measurement uncertainties can be mitigated using hardware or software compensation. Besides, benchmarking conventional and accu-

* Corresponding author at: École de technologie supérieure, 1100, Notre-Dame Ouest, Montréal, H3C 1K3, QC, Canada.
E-mail address: abdelkader.hammouti@etsmtl.ca (A. Hammouti).

https://doi.org/10.1016/j.compfluid.2024.106450
Received 6 April 2024; Received in revised form 5 August 2024; Accepted 4 October 2024
Available online 11 October 2024

rate experimental measurements against CT image-based analysis on the same core sample provides opportunities to develop new methodologies for assessing measurement accuracy and refining methods for reliably estimating porosity using CT scans [5,8].

For permeability calculation, Andrä et al. [9] provide benchmark datasets with several digital images of porous rock microstructures, enabling digital rock simulations at low-Reynolds-numbers. In Andrä et al. [10], results with different numerical methods are compared, revealing variations in permeability values of up to 38% for natural rock samples and approximately 10% for a sample composed of a random sphere pack generated with a Discrete Element Method. Moreover, the irregular shape of convex particles, as studied by Kerimov et al. [11], leads to variations in porosity by 14–25% and corresponding variations in absolute permeability by 45–76%.

A controlled study with reference solutions is crucial to assess gaps in porous media modeling. We propose a methodology using a porous medium with known geometric characteristics to create digital replicas for accurately estimating deviations. Porous media, represented by randomly stacked spherical particles, are deemed "reasonable proxies for sedimentary granular geomaterials" [9]. Additionally, the scientific literature abounds with analytical [12,13], empirical [14,15], and numerical [16,17] studies, often employing monodisperse spheres.

To model porous media flows, we distinguish two numerical methods: boundary-fitted and non-boundary-fitted. The latter includes popular techniques such as lattice-Boltzmann methods [18,19], Immersed Boundary methods [20,21], and Fictitious Domain methods [17,22]. Regardless of methods, a structured Cartesian grid is typically employed. Challenges arise in accurately imposing boundary conditions, necessitating high-order interpolation techniques with sufficient computational points within the pore space to prevent the introduction of numerical errors and ensure local mass conservation [23,24]. Consequently, structured local mesh refinement strategies [25,26] have been explored to automatically enhance refinement in areas of interest, such as narrow regions.

The grid densification in narrow regions originates from boundary-fitted methods, which are especially effective for small pore spaces with well-defined surface boundaries [27,28]. Unstructured hexahedral meshes offer better numerical efficiency, but no general robust automatic mesh generation algorithm exists for porous media studies. Consequently, automated tetrahedral mesh generators are commonly used, as they can produce relatively high-quality meshes with good computational accuracy. However, tetrahedral meshes require more cells to achieve the same computational accuracy as hexahedral grids to ensure good mesh quality and prevent the degradation of computed solution accuracy, especially when flows go through solid particles in contact [29]. Therefore, the best compromise is using hybrid grids combining hexahedral and tetrahedral cells, which are also more suitable for quantifying errors and spatial convergences of solutions

Generating digital replica or twin models from CT data is a genuine challenge, especially to guarantee a high fidelity between the measurement and the sample. Thus, using particles whose geometric characteristics are known a priori allows the direct comparison of the effects of binarization and segmentation on geometric characteristics and the deformations due to image processing and tessellation. The novelty of this study lies in assessing discrepancies generated by a reconstructed 3D digital model, extending from raw CT data to numerical simulations, thanks to the availability of reference solutions that enable convergence studies. Our primary objective is to scrutinize the accuracy in assorted flow regimes by quantifying errors and assessing the spatial convergence of computed solutions.

In Section 2, we recall the main features of our methodology by specifying our modeling workflow, including choices and limitations. In Section 3, we validate our methodology using a well-established configuration with known analytical solutions and numerical extrapolated solutions. Convergence studies are conducted on flows through periodic arrays of spherical particles with different surface treatments to assess the discrepancy of the computed solution. Eventually, in Section 4, we perform numerical simulations of flows through two distinct digital replica models of randomly packed glass beads in a tube generated from CT data.

2. Methodology

To address the methodology accuracy, each process step is split, from CT data to numerical simulations, to determine uncertainty estimations. As described in Fig. 1, four sequences define the framework of this study: (i) Data acquisition and image processing, (ii) geometric modeling, (iii) computational meshing, and (iv) numerical simulation.

2.1. Material

We consider $N_p = 100$ glass beads with a volumetric mass density $\rho_p = 2500$ kg/m^3 and diameter $d_p = 16$ mm with a tolerance $\epsilon_{tol} = \pm 0.3$ mm, contained in a tube of height $L_t = 205$ mm and diameter $D_t = 51$ mm. Given the low measurable polydispersity of beads, we introduce the notion of equivalent sphere diameter by volume, defined as:

$$d_{eq} = \left(\frac{6}{\pi} V_p\right)^{1/3} \tag{1}$$

Bead diameter distribution was assessed through two techniques to establish reference values: (i) d_{mc}, measured using a Mitutoyo Absolute AOS Digimatic caliper (accuracy: ± 0.02 mm). This method is limited to measuring a single diameter in one direction. Additionally, (ii) d_{vb}, representing equivalent sphere diameters by volume V_p, measured with a Sartorius CP124S balance (accuracy: ± 0.1 mg). Both d_{mc} and d_{vb} distributions exhibit similar characteristics, with nearly identical average values ($\langle d_{mc} \rangle = 15.96$ mm, $\langle d_{vb} \rangle = 15.97$ mm) and standard deviations of the same order of magnitude ($\sigma_{mc} = 0.13$, $\sigma_{vb} = 0.15$), below the diameter tolerance ϵ_{tol}. This indicates minimal dispersity, suggesting an imperfectly spherical geometry of beads. Hereafter, the d_{mc} distribution is considered the reference measurement. In the following, the ensemble-averaging operator $\langle \phi \rangle$ and the standard deviation σ_ϕ are defined for a field ϕ as follows:

$$\langle \phi \rangle = \frac{1}{N_p} \sum_{i=1}^{N_p} \phi_i \tag{2}$$

$$\sigma_\phi = \sqrt{\frac{1}{N_p} \sum_{i=1}^{N_p} (\phi_i - \langle \phi \rangle)^2} \tag{3}$$

2.2. Data acquisition and image processing

Data acquisition was conducted at the INRS laboratory using a Siemens Somatom Definition AS CT scanner operating at a voltage of 140 kV and a current of 180 mA. The primary acquisition was performed with a 55 cm field of view, resulting in an image resolution of $h_{vox} = \Delta x = \Delta y = 0.1074$ mm. The reconstructed slice thickness was set to $\Delta z = 0.1$ mm to maintain an isotropic resolution. This approach provides a sharper slice profile in all three directions, thereby enhancing image quality for surface extraction and segmentation. The image reconstruction (IR) was conducted using a Sinogram Affirmed Iterative Reconstruction (SAFIRE, Siemens Healthineers) with a sharp edge-enhancing reconstruction kernel. This IR algorithm is considered as more effective regarding image quality, reducing noise and artifacts [31,32]. Unfortunately, publications related to this commercial software, mainly used as a 'black box', offer minimal information on algorithmic details [33]. While CT metrology can significantly impact accuracy and measurement uncertainty [34,35], it is not within the scope of this paper. This paper only discusses metrics accessed from the volumetric image recorded in DICOM (Digital Imaging and Communications in Medicine) format.

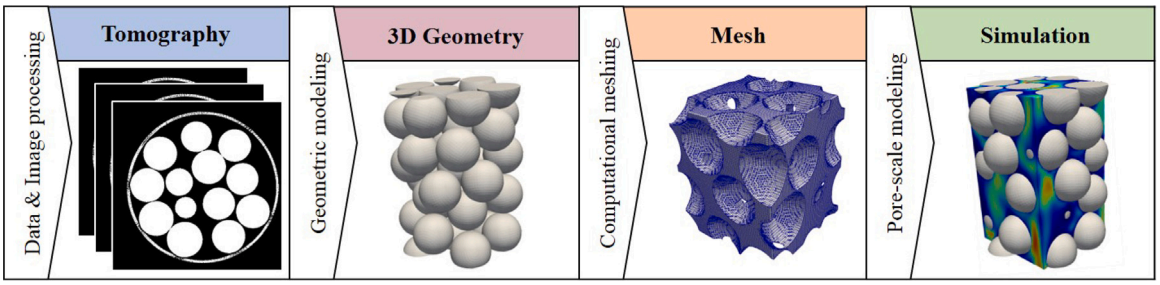

Fig. 1. Workflow for validating our digital rock modeling applied to a glass bead assembly sample.
Source: Adapted from [30].

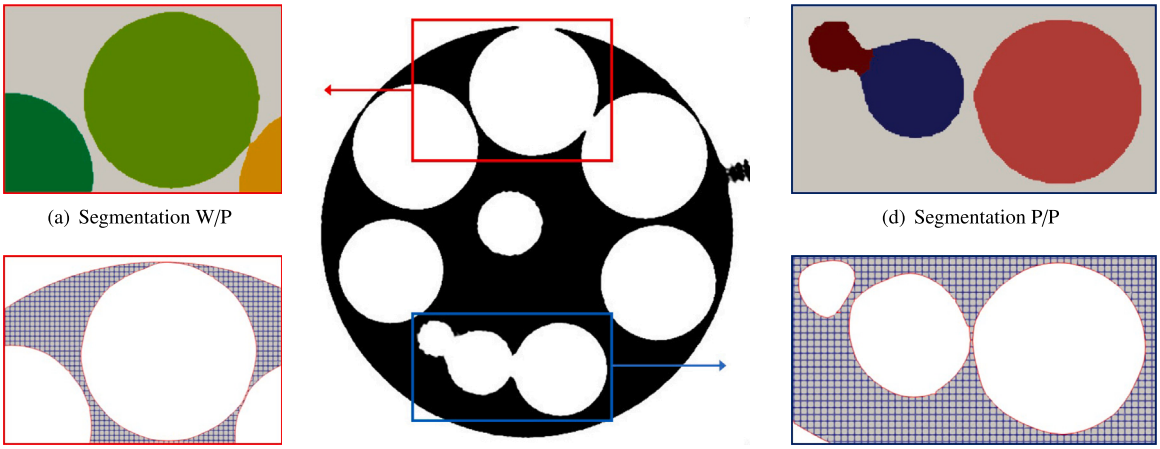

Fig. 2. Various configurations in contact management from a binary image (c): (a) and (b) illustrate segmentation and discretization for bead/wall (B/W) contacts, while (d) and (e) represent bead/bead (B/B) contacts.

2.3. Geometric modeling

Using DICOM files, a segmentation method [36] is applied to convert the Hounsfield Unit (HU)-based volume into a binary-based volume (Fig. 2c). This thresholding technique produces stair-step meshes, introducing an error of the order of h_{vox} on each interface. This initial step is crucial, involving the extraction of a separating surface to build an accurate 3D reconstruction of the original scanned shape in a Standard Triangle Language (STL) format. Segmentation without prior knowledge of the shape is challenging, especially with objects in contact. Therefore, a watershed transform algorithm [37] is utilized to segment contiguous regions into distinct objects (Fig. 2a and d).

Applying the sharpest filter at the level of image acquisition does not necessarily avoid image processing operations, such as using local pre-filtering to overcome aliasing artifacts or erosion/dilation operations to prevent over-segmentation. Therefore, retaining the original geometrical form of scanned objects is a non-trivial task. Using nearly spherical glass beads as a proxy for porous media offers the advantage of individually studying the surface processing applied to each bead to determine and calibrate the deviation margin with reference experimental measurements. Fig. 3 illustrates the various stages of processing the surface to enhance coarsening accuracy, applied to a single scanned bead:

(a) the 3D image segmentation method produces results in binary volumes, and each volume is converted into a surface representation in an STL format (Fig. 3a).
(b) Subsequently, a smoothing filter is applied on the polygonal data set by iteratively adjusting the position of the points (Fig. 3b).
(c) Finally, a decimation filter is added to the previous step to reduce the number of triangles from the original polygonal set (Fig. 3c).

In Fig. 4a, the distribution of diameters d_{mc} measured with a caliper is compared with the distribution of equivalent diameters of binary (or voxel-based) segmented beads, denoted as d_{bin} and referred to as "binarized beads" in the rest of this study. Additionally, it is compared with the distribution of equivalent diameters of smoothed and decimated surfaces applied to the binarized beads, denoted as d_{bsd} and succinctly termed "BSD beads" – an acronym representing Binarization, Smoothing, and Decimation. The binarized and BSD beads' mean and standard deviation values are identical. The deviation of the global average porosity for the 100 binarized and BSD beads is only 0.09%. Additionally, the average values $\langle d_{bin} \rangle$ and $\langle d_{bsd} \rangle$ are slightly lower to $\langle d_{mc} \rangle$. This discrepancy arises from the resolution of contact sizes and segmentation operations. Consequently, the beads' spherical shape is slightly distorted by flattening in the contact areas, as illustrated in Fig. 3. In this assembly, some beads may have up to eight contacts (Fig. 4b). Accordingly, the resolution of contact sizes may significantly influence the discrepancy between binarized and true geometric porosity [11].

To control mesh surface differences after segmentation, smoothing and decimation operations, the Hausdorff distance d_H is used to measure the distance between two meshes X and Y as follows:

$$d_H(X,Y) = \max\{\sup_{x\in X}\inf_{y\in Y} d(x,y), \sup_{y\in Y}\inf_{x\in X} d(x,y)\} \tag{4}$$

Minimizing d_H is a relevant criterion for controlling deviations, commonly used in segmentation and image processing assessments [38] and for training machine learning models as a loss function [39]. In this study, we employ the Hausdorff RMS-distance d_H^{rms} [40], representing the sum of squared distances between pairs of points normalized by the equivalent diameter d_{eq}.

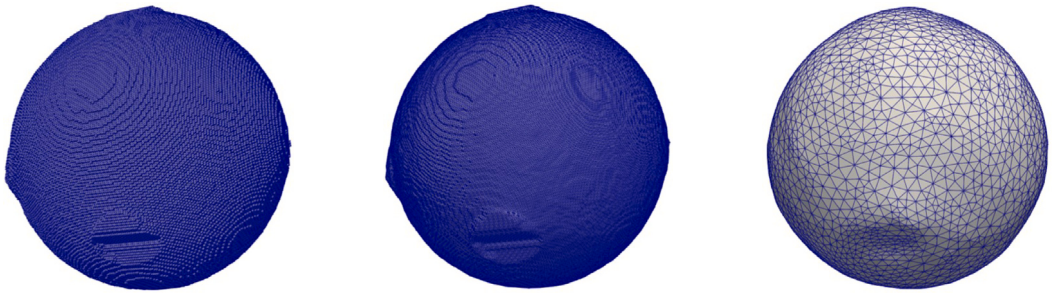

(a) Binarized surface mesh (b) Smooth surface mesh (c) Decimated surface mesh

Fig. 3. The surface processing consists of three stages: (a) an initial binarization process using 223 540 triangles, (b) followed by a smoothing process also employing 223 540 triangles, and (c) concluding with a decimation process resulting in 6704 triangles — showcasing a 97% reduction compared to (b).

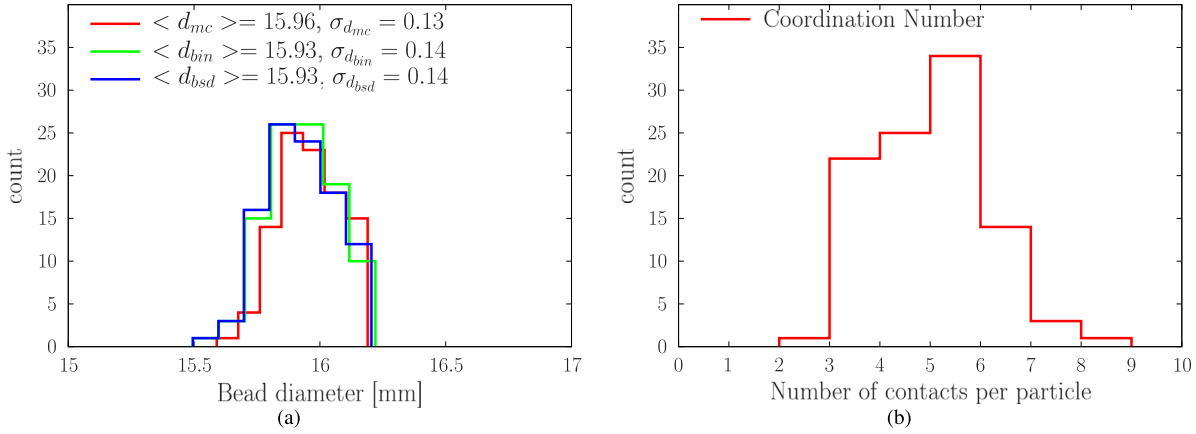

Fig. 4. (a) Comparison of diameter distributions: d_{mc} measured with a caliper, d_{bin} equivalent diameters of base-binary segmented beads, and d_{bsd} equivalent diameters of smoothed and decimated surfaces applied to binarized beads. (b) Number of contacts per particle.

2.4. Computational meshing

The efficient computational mesh corresponds to the porous domain whose limits are precisely defined at the surfaces of the glass beads as well as those of the tube. Alongside geometric modeling considerations discussed earlier, numerical constraints play a crucial role in ensuring solution accuracy and convergence. This includes decisions regarding fluid-solid interaction modeling strategies and treatment of contact points.

Fig. 5 presents typical strategies for modeling fluid/solid boundaries. In configurations with narrow regions from solid/solid contacts, most of the methods (Fig. 5a-b-c) lack sufficient points (blue nodes) to depict the pore space properly and to define the hydrodynamic boundary accurately. These limitations stem from their unfitted boundary nature, relying on interpolation techniques to precisely capture fluid/solid interfaces [17,41].

Achieving mesh convergence in simulations using structured Cartesian meshes often requires mesh sizes as fine as or finer than the original image resolution. According to Guibert et al. [42], even doubling the resolution of a Cartesian mesh may not ensure convergence for permeability. The number of cells discretizing small pore spaces can affect the numerical error in permeability determination. However, increasing the resolution of CT images and meshes to capture finer microstructural details leads to highly computationally demanding simulations.

Unstructured meshes (Fig. 5e) are popular for addressing porous flow in narrow areas, but conducting convergence studies with constant -resolution unstructured meshes is challenging. Automatic mesh generation can result in poorly formed cells in narrow regions, degrading solution quality or causing calculation failures. To our knowledge, no meshing tool efficiently generates complex meshes without producing poor-quality cells within a reasonable time.

Thus, the most effective strategies involve coupling a fluid solver with either a local grid refinement (Fig. 5d) or a hybrid grid (Fig. 5f). Appendix A provides a detailed comparison of numerical results in a configuration with a single particle in a 3-periodic cubic box to evaluate disparities in convergence and accuracy between these meshes. These strategies exhibit at least 2nd-order convergence orders in space for low and high solid volume fractions for diffusive (Fig. A.3) and convective regimes (Fig. A.4). Employing hybrid grids, especially for high solid volume fractions, offers a twofold advantage: it enables a coarser, complex computational domain (other than cuboid in three dimensions) and directs all memory and computational resources exclusively to the cells where the physical processes occur, namely, the pore space.

This study selects a hybrid grid strategy and moderately sized computational domains to ensure that the computational cost associated with grid convergence studies remains tractable. The Body Fitting 3D meshing algorithm, developed in SALOME-platform [43], is utilized here. Similar to a cut-cell-like approach, this algorithm generates regular hexahedrons in the computational fluid part and employs polyhedrons and other types of elements at the intersection of Cartesian cells with geometrical solid boundaries (schematized in Fig. 5f and illustrated with a mesh with a resolution of 36 cells per sphere diameter in Fig. 2b and e). Besides, for the very small cells, a threshold δ is defined to constrain the minimal size of a cell truncated by the geometry boundary; thus, if the size of a truncated grid cell is δ times less than the initial cell size, then the mesh element is not created. In this study, this threshold δ is always larger than 10. Code_Saturne software precalculates various mesh quality criteria, enabling manual cell repairs if needed in post-processing. These criteria measure cell properties like non-orthogonality angles, internal face offset, cell distortion, and volume ratios.

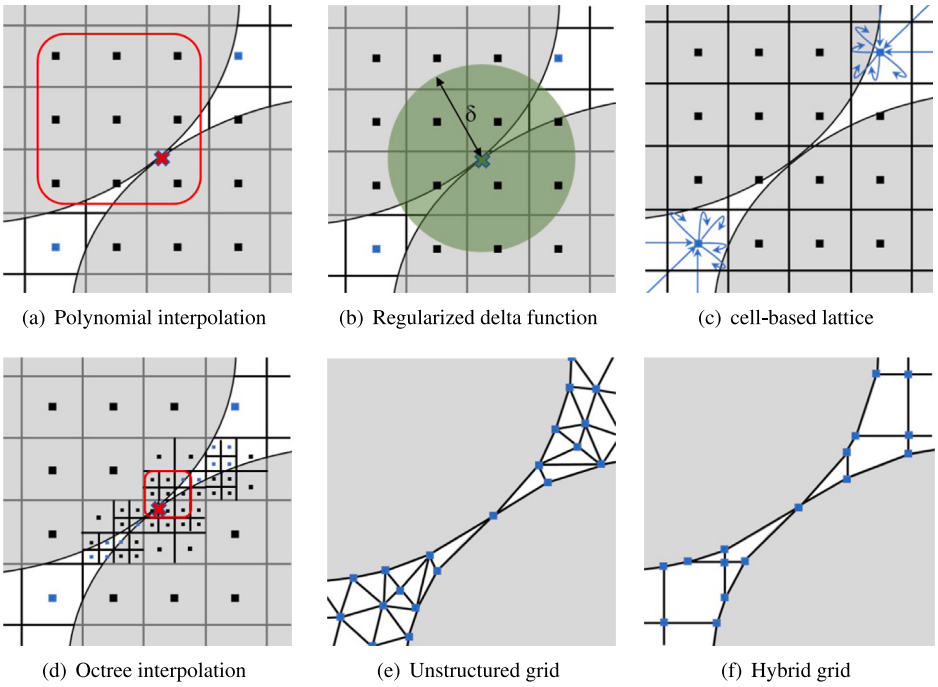

(a) Polynomial interpolation (b) Regularized delta function (c) cell-based lattice

(d) Octree interpolation (e) Unstructured grid (f) Hybrid grid

Fig. 5. Strategies for modeling fluid/solid interactions: (a) 9-point Q2 outwards-oriented interpolation stencil boxed in the red line, (b) centered 3-point regularized delta function in the green circle, (c) boundary handling in lattice-Bolzmann methods, (d) octree interpolation, (e) unstructured grid and (f) hybrid grid. Pore space is shown in white and solid in gray. Blue points are computational nodes in the pore space, and black points are in the solid phase.

The management of these mesh criteria is essential in treating contact points. Indeed, their treatments present significant numerical challenges in porous flows. Achieving a three-dimensional mesh of a closely-packed bed of spheres without geometry modifications is rare [29]. Maintaining mesh quality near contact points is crucial to avoid skewness. Nevertheless, minor changes in sphere or tube wall diameter can notably impact porosity, leading to pressure drop errors. In Appendix B, we demonstrate that a ±1% diameter modification results in approximately 3% void fraction error, leading to pressure drop calculation errors of 7–10% (see Table B.1), consistent with Bai et al. [44].

2.5. Numerical model

Let us consider a domain Ω composed of fluid and solid particles $\mathcal{P}$, of boundary $\partial\Omega$. The governing equations are non-dimensionalized using the following scales: L_c for length, U_c for velocity, $T_c = L_c/U_c$ for time and $\rho_f U_c^2$ for pressure, where ρ_f denotes the fluid density. For this study, we denote dimensionless quantities with a "$*$" superscript. Thus, the dimensionless incompressible fluid flow problem reads as follows:

$$\frac{\partial \boldsymbol{u}^*}{\partial t} + \boldsymbol{u}^* \cdot \nabla \boldsymbol{u}^* = -\nabla p^* + \frac{1}{\mathcal{R}e}\nabla^2 \boldsymbol{u}^*, \quad \text{over } \Omega \tag{5}$$

$$\nabla \cdot \boldsymbol{u}^* = 0, \quad \text{over } \Omega \tag{6}$$

$$\boldsymbol{u}^* = \boldsymbol{0}, \quad \text{over } \mathcal{P} \tag{7}$$

where $\boldsymbol{u}^*$ and p^* represent the dimensionless fluid velocity and pressure, respectively. The particle Reynolds number is defined as follows:

$$\mathcal{R}e = \frac{\rho_f U_c L_c}{\mu_f} \tag{8}$$

where μ_f denotes the fluid viscosity. In the following, the choice for U_c is the far field inlet velocity u_{in}. We choose $L_c = d_p$ where d_p is the particle diameter. Finally, we represent the solid volume fraction by $\alpha_s \in [0, 1]$ and the fluid volume fraction or porosity by $\alpha_f = 1 - \alpha_s$.

The numerical methods employed in Code_Saturne are extensively detailed by Archambeau et al. [45], thus only briefly outlined here. Code_Saturne solves the Navier–Stokes equations for 3D incompressible flows across various mesh types. A fractional step scheme (SIMPLEC) is used to solve the mass and momentum Eqs. (5)–(6)–(7), and relies on a finite volume discretization. The advective terms are treated using a second-order linear upwind scheme and an implicit first order Euler scheme is employed. Finally, incompressibility is satisfied by solving a Poisson equation for pressure correction with a conjugate gradient method preconditioned with K-cycle AMG. The computed error e will be evaluated in terms of the relative deviation of a physical quantity ξ as follows:

$$e(\xi) = \frac{\xi(h) - \xi_{ref}}{\xi_{ref}} \tag{9}$$

where ξ_{ref} represents the reference solution. If no known solution is available, one can establish the solution through numerical consistency by applying the Richardson extrapolation [46] as follows:

$$\xi(h) = \xi_{h\to 0} + \beta h^{\alpha} \tag{10}$$

where $\xi_{h\to 0} = \lim_{h\to 0} \xi(h)$ is the converged solution, α the convergence rate and β the pre-factor of the relative error; h being the grid size. The error $e_{h\to 0}$ is defined as the deviation from the extrapolated solution $\xi_{h\to 0}$:

$$e_{h\to 0}(\xi) = \frac{\xi(h) - \xi_{h\to 0}}{\xi_{h\to 0}} \tag{11}$$

3. Flow through periodic arrays of spheres

To assess the uncertainty of our methodology across various flow scenarios, we perform a stepwise validation, progressing from a geometric representation using parametric equations to a complex geometry described by an STL file obtained from CT data. Flows through an infinite particle packing offer convenient configurations for studying the spatial convergence of computed solutions with mesh refinement. Results are primarily analyzed regarding pressure drop through the porous domain along the streamwise direction or equivalently in terms of friction coefficient K exerted on the solid phase surface (inversely proportional to the permeability coefficient). This investigation spans both viscous and inertial regimes.

3.1. Description

The relation between the mean velocity u_m, the imposed pressure drop Δp in the streamwise direction, and the friction coefficient K for an infinite structured simple cubic array of spheres, modeled as a single sphere centered within a 3-periodic cubic box, is expressed as:

$$\frac{\Delta p}{L} = 18\frac{\mu_f \alpha_s}{d^2} K(\alpha_s, \mathcal{R}e)\, u_m \tag{12}$$

where L represent the cubic box edge length and d the sphere diameter. In Stokes regime, Zick and Homsy [13] provided an analytical development depicting K as a function of the solid volume fraction α_s. This solution lies in its valid domain, up to $\alpha_s^{max} = \pi/6 \simeq 0.524$, enabling the investigation of configurations with high solid volume fractions, such as in a close-packed simple cubic (CSC) array case,

$$\text{for } \alpha_s = \pi/6 \text{ and } \mathcal{R}e \ll 1,\ K_{ref} = 42.1 \tag{13}$$

For finite-Reynolds-number flows, achieving the maximum solid volume fraction α_s^{max} also poses challenges for various numerical methods (see Section 2.4). However, no analytical solution is available. In Appendix A, the spatial convergence of the computed solution with grid size is assessed using a reference solution K_{ref} obtained by extrapolation to zero grid size [46], as follows:

$$\text{for } \alpha_s = \pi/6 \text{ and } \mathcal{R}e = 54,\ K_{ref} = 54.3 \tag{14}$$

In all simulations, spheres are enclosed in a 3-periodic cubic box such as $L = d_p = 1$. The spatial resolution is uniform in all directions, with $N_x = N_y = N_z$, resulting in a grid size $h^* = 1/N_x$. The fluid viscosity is set to $\mu_f = 1.25 \times 10^{-2}$ Pa s and the imposed pressure drop Δp is adjusted to achieve $\mathcal{R}e \sim 0.01$ and $\mathcal{R}e = 54$.

3.2. Ideal sphere generated by parametric equations

Ideal spheres are commonly used for validating and assessing the convergence and accuracy of numerical methods [47,48]. This section outlines two approaches for surface representation: parametric shape and parametric mesh.

3.2.1. Ideal sphere surface described by a parametric shape

In computational geometry, parametric shapes are fundamental geometric primitives that utilize mathematical representations to describe geometric objects' form and features with a minimal set of parameters. Ideal spheres are chosen as parametric shapes due to their analytically defined surfaces, minimizing additional approximations. This setup enables us to assess how high solid volume fractions and particle–particle contact points impact the numerical resolution. As discussed in Appendix A, practical configurations like densely concentrated spheres with multiple contacts can adversely impact the expected convergence order (see Fig. A.3b). Employing a hybrid mesh with an efficient fluid solver ensures constant convergence rates and relatively stable accuracy across varying solid volume fractions α_s (see Fig. A.2b).

In a CSC array of spheres, our numerical results in the Stokes regime converge towards a friction coefficient $K_{h\to 0} = 42.1$. The agreement with the analytical solution Eq. (13), proposed by Zick and Homsy [13], is very satisfactory. For moderate-Reynolds numbers, we conduct simulations with varying Reynolds numbers (up to $\mathcal{R}e = 54$) and grid resolutions (up to $h^* = 1/128$) to establish the coefficient K as h approaches zero. The comparison of our computed solutions with highly accurate numerical solutions shows a good agreement (details in Appendix A.2).

In Fig. 6, we investigate the configuration of a CSC array of spheres by examining the accuracy and convergence of our computed solutions for $\mathcal{R}e \ll 1$ and $\mathcal{R}e = 54$. For $\mathcal{R}e \ll 1$, we observe a clean spatial 2nd-order convergence with a rate $\alpha = 1.8$, even in the near-contact region where the mesh can be strongly non-orthogonal. For $\mathcal{R}e = 54$, the grid resolution affects convective flux reconstruction. The convergence rate α falls to 1.6, deemed satisfactory for a second-order accurate scheme. The deviations e between computed and reference solutions remain below 4% for grid resolutions $h^* \leq 1/32$.

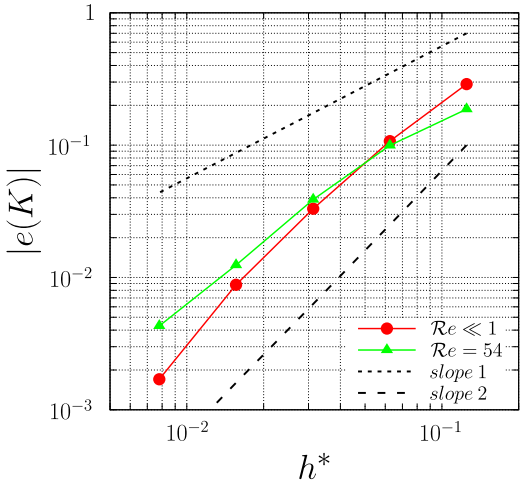

Fig. 6. Convergence study of computed solutions for flows through an infinite structured cubic-centered array of ideal spheres defined by a primitive surface in the configuration of CSC array of spheres: Variation of relative deviations e with the analytical solution Eq. (13) proposed by Zick and Homsy [13] for $\mathcal{R}e \ll 1$ and with the reference solution for $\mathcal{R}e = 54$ defined by Eq. (14).

3.2.2. Ideal sphere surface described by a STL file

This section explores the impact of tessellation on a spherical surface to assess the computed solution's convergence and accuracy. Achieving an even distribution of points on a sphere is a challenging problem in geometry [49]. The uniformity of point distribution on the sphere's boundary significantly influences convergence outcomes [17,50]. Two configurations are presented to generate a discrete set of points on the sphere's surface and reconstruct a surface mesh:

1. An uneven distribution of points, termed the (θ, φ)-distribution, is characterized by the θ-resolution, N_θ, representing the number of points on cross sections of the sphere in the XY plane. The φ-resolution, N_φ, corresponds to the number of points (excluding the poles) on the cross sections of the sphere in the XZ plane. Four resolutions are considered $N_\theta = N_\varphi = N_{\theta,\varphi} = \{8, 16, 32, 64\}$ corresponding to the quantities of triangles defining the surface mesh $N^u_{tri} = \{96, 448, 1920, 7936\}$.
2. An even distribution of points, known as the Fekete distribution [51], is achieved by configuring points to minimize the total repulsive energy in a system of charged particles. Physically, this energy corresponds to the interactions of N^e_{pts} charged point-particles as they repel each other according to Coulomb's law. Subsequently, the Ball Pivoting algorithm [52] is applied to generate a triangle mesh using the provided point cloud N^e_{pts} such as $N^e_{tri} = N^u_{tri}$.

Four surface resolutions are generated in an STL format with two different point distributions: (θ, φ)-distribution in Fig. 7-top and Fekete distribution in Fig. 7-bottom. The Hausdorff RMS-distance is computed for each configuration compared to a highly resolved surface sphere. For uneven and even point distributions, maximum deviations are measured at $N^u_{tri} = N^e_{tri} = 96$ with a value of 2.4%, and 1.9% respectively. Conversely, minimum deviations are observed at $N^u_{tri} = N^e_{tri} = 7936$ with 0.02% and 0.01% respectively.

To analyze the simultaneous influence of surface mesh resolution $h^*_{tri} = 1/\sqrt{N_{tri}}$ and the volume mesh resolution h^* on the friction coefficient K, the convergence of the computed solution is plotted for

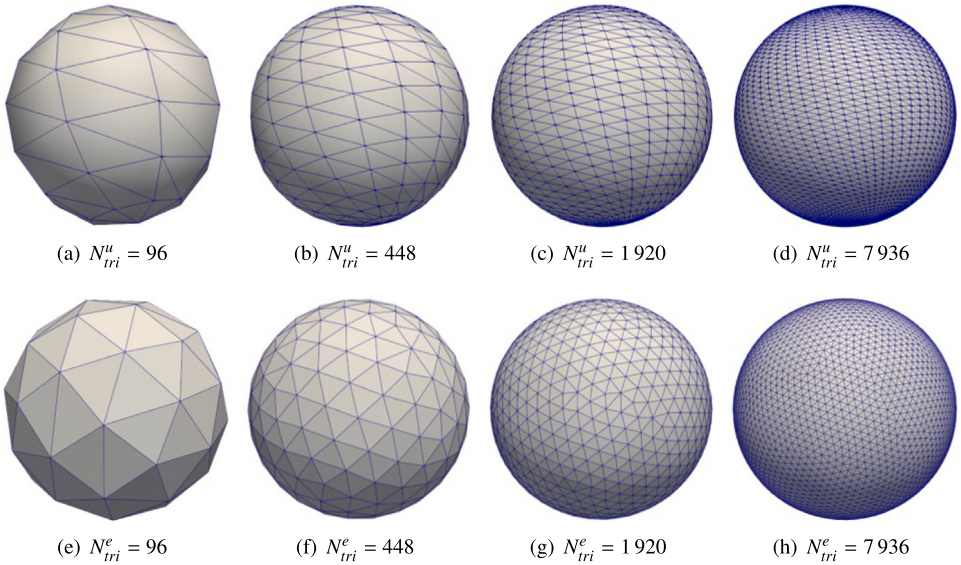

(a) $N^u_{tri} = 96$ (b) $N^u_{tri} = 448$ (c) $N^u_{tri} = 1\,920$ (d) $N^u_{tri} = 7\,936$

(e) $N^e_{tri} = 96$ (f) $N^e_{tri} = 448$ (g) $N^e_{tri} = 1\,920$ (h) $N^e_{tri} = 7\,936$

Fig. 7. Comparison of two surface triangulations: on top, generated from the uneven (θ, φ)-distribution, and on the bottom, generated from the even Fekete distribution. Four grid resolutions are shown with: (a)–(e) 96 triangles, (b)–(f) 448 triangles, (c)–(g) 1920 triangles, and (d)–(h) 7936 triangles.

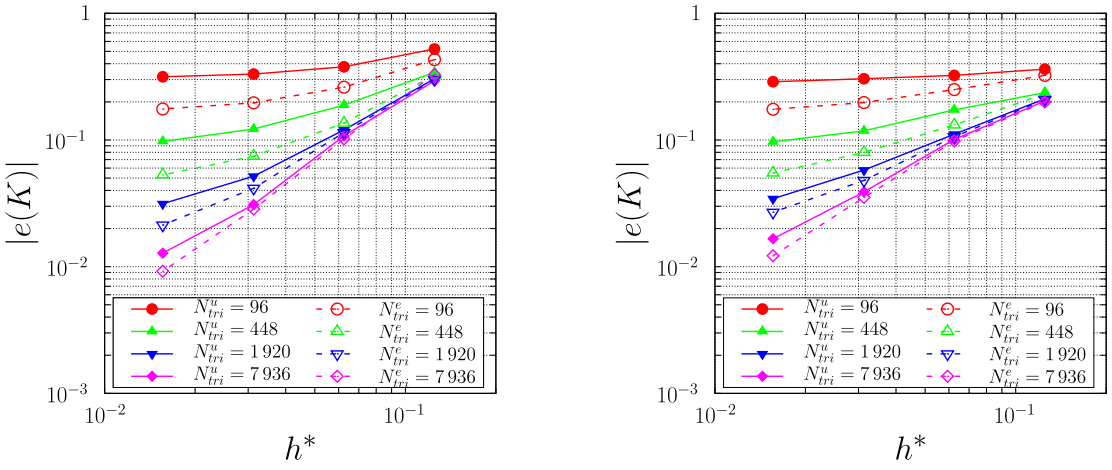

(a) $\mathcal{R}e \ll 1$ (b) $\mathcal{R}e = 54$

Fig. 8. Convergence and evolution study of computed solutions for flows through an infinite structured cubic-centered array of spheres, exploring the influence of the number of triangles on unevenly distributed points N^u_{tri} and evenly distributed points N^e_{tri} on the surface of an ideal sphere. The numerical results are compared with (a) the analytical solution Eq. (13) for $\mathcal{R}e \ll 1$ and (b) the reference solution defined by Eq. (14) for $\mathcal{R}e = 54$.

$\mathcal{R}e = 0.01$ and $\mathcal{R}e = 54$ in Fig. 8. The overall trend indicates that as the number of triangles increases from 96 (i.e. $h^*_{tri} \sim 10^{-1}$) to 7936 (i.e. $h^*_{tri} \sim 10^{-2}$), the convergence rate α also increases. This result demonstrates the very significant influence of the size of the surface mesh triangles, i.e. when h^*_{tri} is larger or similar to h^*, it dominates the deviation.

The discretization of a simple geometry like a sphere can be influenced by various choices, leading to significant deviations in convergence and accuracy. An even distribution of points on an extracted surface yields the best results. Higher resolution brings the approximation closer to an ideal sphere but comes with an increased computational cost. Therefore, a significant challenge in DRP is finding the optimal trade-off between grid size and the minimum number of triangles required for satisfactory numerical accuracy while managing computational cost. Hereafter, a minimum of 6000 triangles describe particle surfaces.

3.3. Binarization, Smoothing and Decimation (BSD) of an ideal sphere

To closely replicate the geometric modeling applied on a surface extracted from CT-scan imaging (Fig. 3), we begin by evaluating deviations with an ideal sphere that undergoes a process of binarization, followed by smoothing and decimation. Computational runs are conducted at each phase to compute the friction coefficient K and assess resulting discrepancies.

To evaluate the effects of spatial resolution anisotropy on K, a convergence analysis is achieved at $\mathcal{R}e \ll 1$ and $\mathcal{R}e = 54$, using a binarized ideal sphere with a $100 \times 100 \times 25$ voxel mesh resolution (a standard resolution for medical CT-scan detectors). The analysis reveals a deviation on K of approximately 1% for a z-direction flow and a discrepancy ranging from 4% to 5% in the x- and y-direction flows. Therefore, isotropic spatial resolutions are strongly recommended to minimize the uncertainties. Subsequently, we examine the binarization of an ideal sphere with a $100 \times 100 \times 100$ voxel mesh resolution. The convergence with respect to h^* is depicted in Fig. 9 for both regimes, showing almost second-order convergence. It is worth noting that the

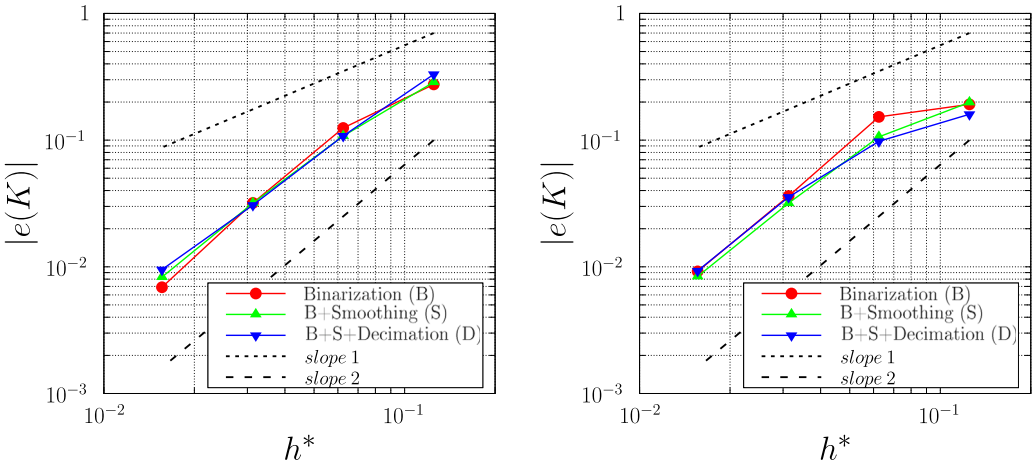

(a) $\mathcal{R}e \ll 1$ (b) $\mathcal{R}e = 54$

Fig. 9. Convergence study of the friction coefficient K as a function of grid size h^* and applied processes on the surface of an ideal sphere: Binarization with a $100 \times 100 \times 100$ voxel mesh resolution (B), Binarization and Smoothing (BS) and Binarization, Smoothing and Decimation (BSD). The numerical results are compared with (a) the analytical solution Eq. (13) for $\mathcal{R}e \ll 1$ and (b) the solution reference defined by Eq. (14) at $\mathcal{R}e = 54$ for the case of the flow through an infinite structured cubic-centered array of spheres.

Table 1
Geometric features resulting from various surface processing techniques.

	nb triangles	Surface	Volume	d_{eq}	d_H^{rms} (%)
Ideal sphere	–	π	$\pi/6$	1.000	–
Binarization (B)	94 320	4.716	0.524	1.000	0.439
B+Smoothing (S)	94 320	3.148	0.525	1.000	0.083
B+S+Decimation (D)	6000	3.140	0.525	1.000	0.097

binarized sphere surface is about 50% larger than that of an ideal sphere (Table 1). While binarized surfaces exhibit the potential for direct use as a surface mesh, particularly in microtomography [53], a drawback is the substantial memory allocation it demands.

Consequently, to enhance coarsening accuracy, we initially apply a smoothing filter [54]. This filter adjusts point coordinates using Laplacian smoothing, relaxing the mesh and resulting in better-fitted cells with a more evenly distributed point distribution. Finally, a decimation filter [55] is applied on the smoothed surface, reducing the number of triangles from 94 320 to 6000. This algorithm preserves the topology with an excellent approximation, yielding $d_H^{rms} \sim 0.1\%$ (Table 1). As a result, it leads to nearly identical convergence between an ideal sphere and a sphere subjected to BSD processes.

3.4. Glass bead generated from CT data

We randomly select a single bead reconstructed from CT data. This bead results from binarization and segmentation of the 100-bead assembly detailed in Section 2.3. Then, we apply surface processing techniques (Section 3.3). The segmentation operation induces geometric deformations, resulting in a slightly anisotropic shape with flattened areas on the surface, especially in the contact point regions (Fig. 10). The Hausdorff distance between the surface mesh of this bead and an ideal sphere is $d_H^{rms} = 0.4\%$.

We study the convergence of the computed solutions for flows through an infinite structured cubic-centered array of a single bead reconstructed from CT data for two different regimes as illustrated in Fig. 11. By successively imposing three flow directions, we compare the friction coefficients (K^x, K^y, K^z) with the analytical solution $K_{ref} = 42.1$ at $\mathcal{R}e \ll 1$ (Fig. 12a) and with the numerical reference solution $K_{ref} = 54.3$ at $\mathcal{R}e = 54$ (Fig. 12b). The convergence is not entirely smooth, mainly attributed to the anisotropic nature of the tested bead, significantly influencing the friction coefficient in the x, y, and z flow directions. The extrapolation values of (K^x, K^y, K^z) as the grid size h approaches zero (Fig. 12c and d) show deviations of $(-2.4\%, 0.7\%, -0.2\%)$ for $\mathcal{R}e \ll 1$ and $(-2.2\%, 1.1\%, -0.4\%)$ for $\mathcal{R}e = 54$ compared to the friction coefficient of an ideal sphere.

4. Flow through random arrays of glass beads

In this section, we transition from a theoretical case of an infinite domain with identical particles to a practical scenario involving a finite domain with real geometry reconstructed from CT data. The focus is on fluid flow through a random packing of glass beads, considering the influence of confining walls on the permeability.

4.1. Description of digital replica models

Two digital replica models are built to accurately reflect the assembly of 100 randomly distributed glass beads, as follows:

- The first digital replica model, DRM_1, is generated from geometrical data (gravity center positions and equivalent diameters) extracted from CT data to model an assembly of 100 ideal spheres. To ensure mesh quality, a 0.2% reduction in the diameter of each sphere is applied to prevent highly skewed cells. For all spherical particles $i \in \mathcal{P}$, diameters are set as $d_1[i] = 0.998 d_{bsd}[i]$.
- The second digital replica model, DRM_2, is constructed from the surfaces of each bead extracted from CT data in STL files. These surfaces are binarized, segmented, and smoothed, outlined in Section 3.3. Bead surfaces are then decimated to approximately 6000 triangles. No further size adjustments are made, i.e. $\forall i \in \mathcal{P}$, we set $d_2[i] = d_{bsd}[i]$.

To set up the CFD simulations, the tube wall is modeled as a bounding cylinder with a diameter of D, enclosing all beads. This constraint ensures that the averaged solid volume fractions in each computational mesh closely match those derived from the original geometric data after binarization and BSD processing. It also prevents skipping too many cells in the Bead/Wall contact areas, detailed in Appendix B. The tube-to-particle diameter ratio is set at $D/d_p = 3.23$. The tube length is $L = 12.81 d_p$, and both the inlet and outlet zones are kept free of beads, each having a length of $L_{in} = L_{out} = d_p$ as presented in Fig. 13a. To mitigate entrance effects [56], the first two layers and the last layer of particles in the bed along the streamwise direction are consistently excluded in our analysis. The boundary conditions are set as follows: no-slip conditions on the cylinder wall and bead surfaces,

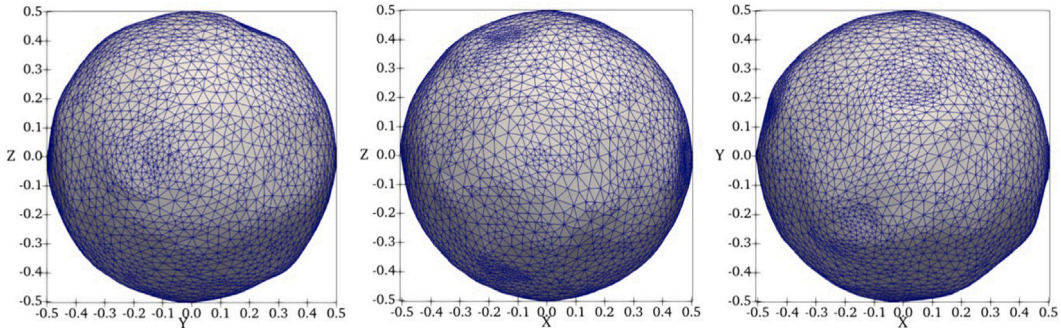

(a) YZ-plan (b) XZ-plan (c) XY-plan

Fig. 10. Three views of a selected glass bead reconstructed from CT data (normalized by the equivalent diameter d_{eq}) following binarization, segmentation, smoothing and decimation processing with 6704 triangles: (a) YZ-plan, (b) XZ-plan, and (c) XY-plan.

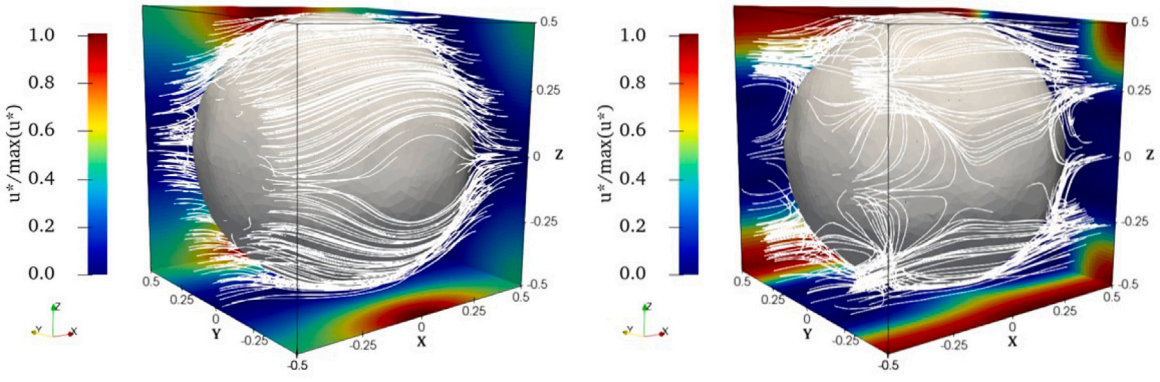

(a) $\mathcal{R}e \ll 1$ (b) $\mathcal{R}e = 54$

Fig. 11. Streamlines and velocity contours as the fluid flows from left to right through a YZ-plane (refer to Fig. 10(a)) for a selected glass bead reconstructed from CT-scan data after binarization, segmentation, smoothing, and decimation processes with 6704 triangles at (a) $\mathcal{R}e \ll 1$ and (b) $\mathcal{R}e = 54$.

a uniform upward inlet velocity u_{in} at the bottom of the tube, and a zero-pressure outlet condition at the top.

We compare our numerical results with an empirical correlation introduced by Reichelt [15]. Specifically designed for the configuration of a monodisperse sphere assembly with a tube-to-particle diameter ratio $D/d_p < 10$, the correlation is expressed in dimensionless form as follows:

$$\frac{\Delta p^*}{L^*} = \frac{\alpha_s}{(1-\alpha_s)^3} f_K(\alpha_s, \mathcal{R}e) \tag{15}$$

where

$$f_K(\alpha_s, \mathcal{R}e) = \left(K_1 A_w^2 \frac{\alpha_s}{\mathcal{R}e} + \frac{A_w}{B_w} \right) \tag{16}$$

with the wall correction terms $A_w = 1+2/(3(D/d_p)\alpha_s)$, $B_w = \left[k_1(d_p/D)^2 + k_2\right]^2$ and in the case of spheres, $(K_1, k_1, k_2) = (154, 1.15, 0.87)$.

4.2. Results

To study the convergence and accuracy of our two digital replica models, we conduct numerical simulations at $\mathcal{R}e = 0.01, 32, 64$, and 96 (examples illustrated in Fig. 14). For each $\mathcal{R}e$ case, we assess the spatial convergence of the computed solution f_K by analyzing the pressure drop convergence with mesh refinement, varying from $h^* = 1/8$ to $1/50$. To accurately determine the pressure drop, we discretize the domain into layers spanning the entire tube in the xy-direction, each with a height of Δz in the z-direction. For each simulation, we ensure that the axial profile of the pressure $\langle p^* \rangle_z$ exhibits no inlet-outlet boundary effects as shown in Fig. 13b. Additionally, we compute the deviation ε_{α_s} between the overall averaged solid volume fractions for each h^*-size mesh and the corresponding values obtained for the binarized beads (similar results with the BSD beads). Except for the coarsest grid size $h^* = 1/8$ where $\varepsilon_{\alpha_s} \simeq 4\%$, we observe a reasonable deviation ε_{α_s} ranging approximatively between 0.2% and 1.2% for DRM_1 and 0.3% and 0.7% for DRM_2.

In Fig. 15a and b, we observe nearly identical convergence for both cases, DRM_1 and DRM_2. This outcome highlights the efficiency of the surface reconstruction technique, including smoothing and quadratic decimation with approximately 6000 triangles per bead in the DRM_2. A stable convergence is reached from $h^* = 1/16$. For the grid size $h^* = 1/50$, the deviations are within the range of 1% to 3% for DRM_1 and DRM_2. In Table 2, we compare the deviation between the extrapolated numerical solutions $f_{K,h\to 0}$, obtained using Richardson extrapolation, for the two digital replica models DRM_1 and DRM_2 with Reichelt [15]'s empirical correlation (Eq. (15)). The deviations range between -1.2% and 1.7% for DRM_1 and between -0.8% and 2.8% for DRM_2. These minimal discrepancies in friction coefficients between DRM_1 and DRM_2, are likely due to the 0.02% shrinkage of sphere diameters in DRM_1. Furthermore, these results suggest that in configurations with minimal size dispersity and particle deformations, using ideal spheres to mimic a real packed bed is entirely relevant.

5. Conclusions

In this study focusing on the uncertainty assessment of Digital Rock Physics, we introduced a methodology with a qualitative framework. Reference solutions were employed to evaluate deviations from CT data in pore-scale simulations. We accomplished this goal by providing a precise representation of the pore-particle geometry through an investigation into the influence of surface extraction on geometric modeling

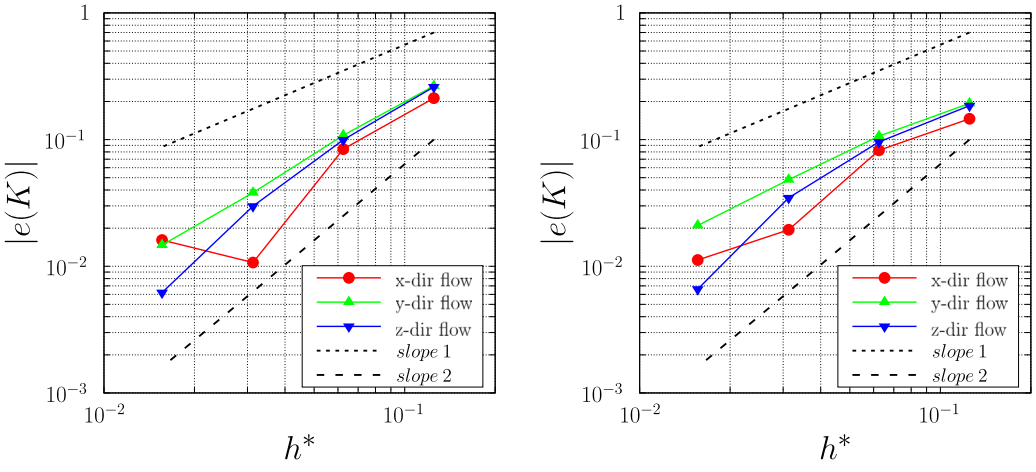

(a) $\mathcal{R}e \ll 1$, $K_{ref} = 42.1$ in all directions

(b) $\mathcal{R}e = 54$, $K_{ref} = 54.3$ in all directions

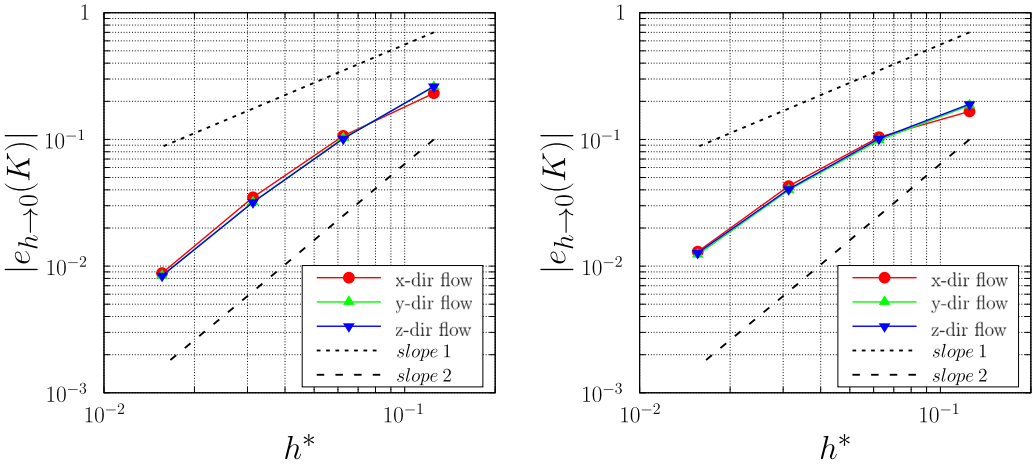

(c) $\mathcal{R}e \ll 1$, $(K^x_{h\to 0}, K^y_{h\to 0}, K^z_{h\to 0}) = (43.1, 41.8, 42.2)$

(d) $\mathcal{R}e = 54$, $(K^x_{h\to 0}, K^y_{h\to 0}, K^z_{h\to 0}) = (55.6, 53.8, 54.6)$

Fig. 12. Convergence study of computed solutions for flows through an infinite structured cubic-centered array of beads reconstructed from CT data, in x-, y- and z-directions (illustrated in Fig. 10). The friction coefficient K is compared with (a) the analytical solution $K_{ref} = 42.1$ for $\mathcal{R}e \ll 1$, (b) the numerical reference solution from Eq. (14) $K_{ref} = 54.3$ for $\mathcal{R}e = 54$. Then as h^* approaches zero with $(K^x_{h\to 0}, K^y_{h\to 0}, K^z_{h\to 0})$ equal to (c) $(43.1, 41.8, 42.2)$ for $\mathcal{R}e \ll 1$ and (d) $(55.6, 53.8, 54.6)$ for $\mathcal{R}e = 54$.

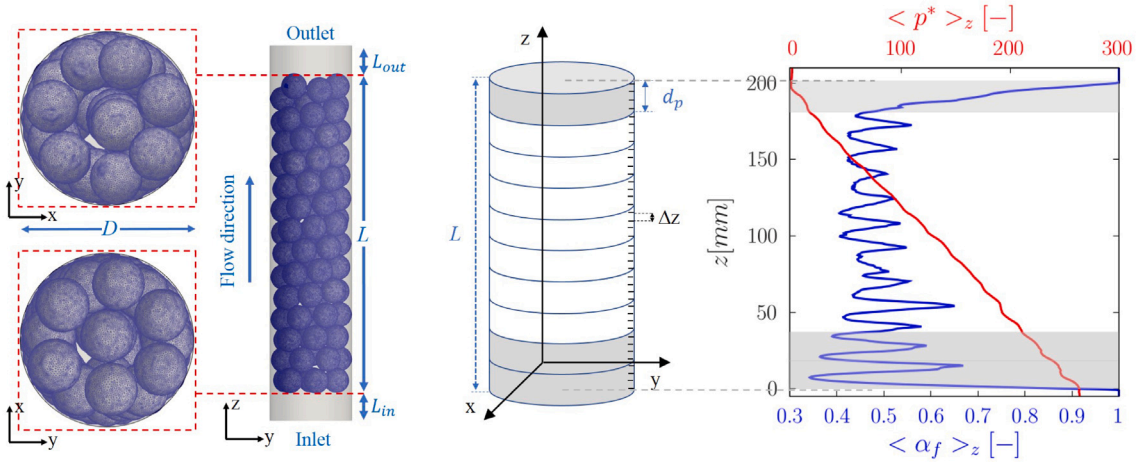

(a) Computed domain description

(b) Z-averaged-pressure and z-averaged-fluid volume fraction profile

Fig. 13. Schematic overview of (a) the digital replica model (DRM_2) and boundary definitions used in Code_Saturne and (b) post-processing numerical data, including the decomposition of the domain into Δz-layers and an example of output resulting from averaging on the digital replica.

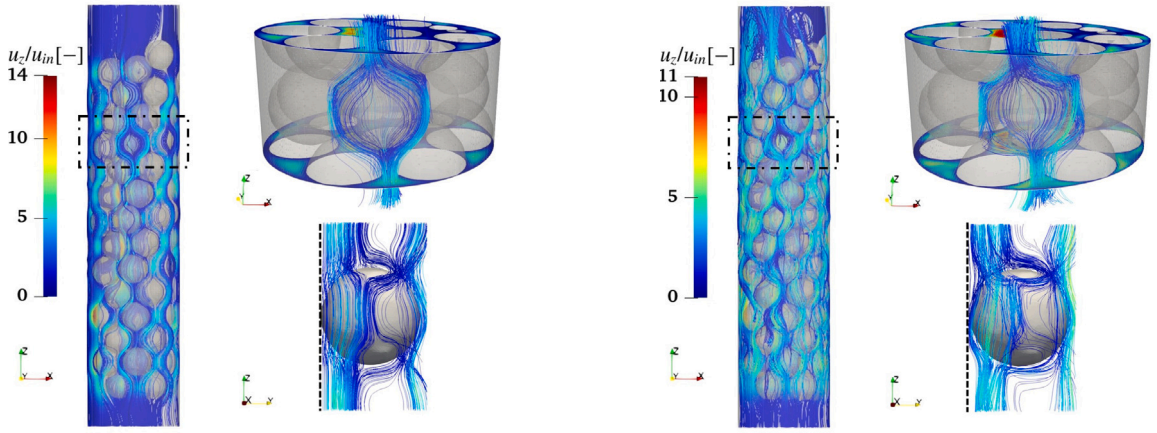

(a) Stokes flow ($Re \ll 1$) (b) Moderate-Reynolds-number flow ($Re = 96$)

Fig. 14. Different section views of 3D flow fields using streamlines of normalized velocity with the digital replica model DRM_2 and a resolution $h^* = 1/50$ at (a) $Re \ll 1$ and (b) $\mathcal{R}e = 96$.

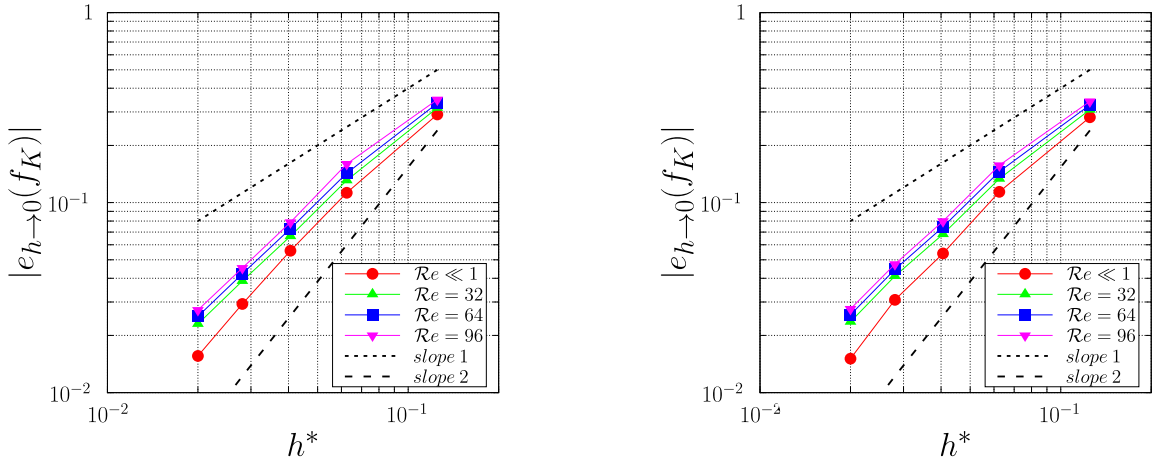

(a) DRM_1 (b) DRM_2

Fig. 15. Study of convergence of the computed solution from Code_Saturne results compared with the correlation Eq. (15) by Reichelt [15] for $\mathcal{R}e \ll 1$, $\mathcal{R}e = 32$, $\mathcal{R}e = 64$ and $\mathcal{R}e = 96$ for flows through a random packing structure of spheres confined in a cylindrical tube for (a) the digital replica model with ideal spheres (DRM_1) and (b) the digital replica model with glass beads generated from CT data via STL files (DRM_2).

Table 2
Comparison of the deviation between the Reichelt [15]'s empirical correlation (Eq. (15)) with the extrapolated numerical solution $f_{K,h\to 0}$ for the two digital replica models with 100 ideal spheres (DRM_1) and 100 reconstructed glass beads (DRM_2).

Configurations	Deviation $e(f_{K,h\to 0})$			
	$\mathcal{R}e \ll 1$	$\mathcal{R}e = 32$	$\mathcal{R}e = 64$	$\mathcal{R}e = 96$
DRM_1	−0.012	−0.008	0.012	0.017
DRM_2	−0.008	0.003	0.024	0.028

coupled with a hybrid mesh. The methodology has been validated through an analytical solution for the Stokes regime and a numerical reference solution for moderate-Reynolds numbers in the context of flows through an infinite structured cubic-centered array of spherical particles (Section 3). Finally, a mesh convergence study was conducted on two digital samples of a glass beads assembly: the first, DRM_1, utilizes geometrical characteristics from CT data, assuming beads are ideal spheres. The second, DRM_2, involves extracting and processing bead surfaces from CT data via STL files (Section 4).

This methodology enables the accurate assessment of uncertainties during the construction of replica digital models. It is achieved by investigating, at each stage, the effects of various modeling choices, including the parameters of segmentation, geometrical modeling, and mesh computation. The precise definition of the geometric characteristics of the porous medium plays a crucial role in calculating porosity and, consequently, pressure drop. In investigating various configurations of sphere surfaces within the context of flow through a structured array of particles, we found that a minimum of 6000 uniformly tessellated triangles is required to accurately represent the surface of a sphere defined in STL format, ensuring mesh convergence for pressure drop calculations. Additionally, we demonstrated that a mere 1% modification in particle diameter can induce a 3% deviation in solid volume fraction, subsequently causing a 7–10% error in pressure drop prediction for different flow regimes ($\mathcal{R}e \ll 1$ and $\mathcal{R}e = 54$). Using a hybrid grid allows for the effective treatment of issues arising from contact points by mitigating cell skewness or, in the worst-case scenario, shrinking the particles' diameters to a minimum. In a digital replica model using surface geometry from CT data, segmentation impacts particle shape by slightly flattening contact areas, benefiting mesh generation and permeability computation. These findings on packings of (nearly ideal) spheres will serve as guidelines or technical recommendations to handle real geomaterials and reduce errors. Indeed, with micro-CT data, this approach is applicable by gradually increasing the complexity of rocks with microstructures primarily composed of

convex grains, such as sand pack or sandstone. The non-convexity of the grains can be challenging during segmentation but can be handled with numerical simulations [57]. In these configurations, only experimental data can assess the uncertainty of the digital rock model. This includes porosity measurements (e.g., 3D porosity matrices [5]) for checking the 3D geometry and permeability measurements for validating the numerical simulations.

Eventually, this methodology is extensible to multi-physical processes such as heat transfer [56] or mass transfer [58]. In such couplings, careful consideration of spatial resolution is crucial to capture the thickness of mass and thermal boundary layers, especially in inertial regimes, where these layers are finer than their hydrodynamic counterparts.

CRediT authorship contribution statement

Abdelkader Hammouti: Writing – review & editing, Writing – original draft, Visualization, Supervision, Software, Methodology, Conceptualization. **Fatna Oukaili:** Visualization, Software, Methodology. **Damien Pham Van Bang:** Writing – review & editing, Supervision, Software, Methodology.

Declaration of competing interest

The authors declare the following financial interests/personal relationships which may be considered as potential competing interests: Damien Pham Van Bang reports a relationship with Natural Sciences and Engineering Research Council of Canada that includes: funding grants. Damien Pham Van Bang reports a relationship with Compute Canada that includes: funding grants. If there are other authors, they declare that they have no known competing financial interests or personal relationships that could have appeared to influence the work reported in this paper.

Data availability

Data will be made available on request.

Acknowledgments

The authors would like to acknowledge ComputeCanada (project SINAPSE, No. 3148 and project ESPRIL, No. 4516) for providing access to the computing facility and the NSERC-Discovery, Canada program (RGPIN-2018-0677) for additional support. The authors would like to thank L.-F. Daigle and P. Letellier for their contribution to the collection of CT-scan data.

Appendix A. Accuracy of numerical results for flows past a structured simple cubic array of spheres from dilute to maximum packing

Uniform Cartesian grids have proven exceptionally successful for over two decades with the simultaneous advancement of high-performance computing (HPC) and sophisticated interface interpolation algorithms considering fluid/solid interactions. Notable methods within this framework include the Ghost Fluid method [59], Immersed Boundary method [60], and Fictitious Domain [22]. However, implementing a numerical method on a regular Cartesian grid, although having numerous advantages associated with constructing its matrix operators (enabling accelerated convergence of iterative solvers, employing lightweight data structures, and supporting straightforward domain decomposition for parallelization), entails certain limitations. A noticeable limitation pertains to the inherent simplicity of its computational domain, typically a cuboid in three dimensions. Besides, these methods are well suited in dilute and moderately dense configurations. Nevertheless, many are inefficient for high solid volume fractions [17,61]. Indeed, the higher the resolution in the porous space for accuracy purposes, the greater the need for memory and computational resources. Additionally, many computational cells are found within the solid phase, allocating significant memory and computational resources to these cells where no physical processes occur. Recent works on structured Adaptative Mesh Refinement (AMR) strategies [62] attempt to address these problems by increasing the level of refinement in contact point regions (areas of interest for flows in porous medium) and by decreasing it in the solid phase.

In Fig. A.1, three examples of meshes are compared for the case of a single sphere in a 3-periodic cubic box, i.e., the solid particle has six contact points with six other particles. Regarding the number of elements N_{elts} for a dense configuration where the particle represents a solid volume fraction $\alpha_s = \pi/6$ equivalent of 52.36% of the solid volume occupied in the volume box. In this configuration, the hybrid grid has ∼38% fewer elements than the uniform grid and ∼20% fewer elements than the octree, as equivalent resolution.

A.1. Stokes flows

The study of Stokes flows through an infinite structured cubic-centered array of spheres at $\mathcal{R}e < 1$ is commonly used as a validation test-case to assess the convergence and accuracy of an implemented numerical method [17,48,63]. We first test the solution computed by Code_Saturne using a hybrid grid with a dimensionless space step $h^* = 1/32$ and time step $\Delta t^* = 0.05$. Fig. A.2a shows the evolution of the computed friction coefficient K as a function of the solid volume fraction α_s with the analytical solution supplied by Zick and Homsy [13] up to $c_s^{max} = \pi/6$. This plot demonstrates a satisfactory agreement between the numerical results and the analytical solution, with a deviation of less than 4%. We additionally assess the accuracy of our computed solution in Fig. A.2b by depicting its convergence relative to the dimensionless grid size h^*. The results exhibit a clean spatial convergence for all α_s with a rate convergence $\alpha \in [1.7 : 1.9]$, and the error e increases slightly with the solid volume fraction α_s.

In Fig. A.3, we compare the computed solutions, ranging from dilute to maximum packing, with the analytical solution proposed by Zick and Homsy [13]. The comparisons are performed on four different grids: uniform and octree grids using basilisk code [64] and hybrid and tetrahedral grids using Code_Saturne [45]. All computed solutions exhibit clean spatial convergences. As expected, the uniform grid is less accurate than octree or hybrid grids, especially at low resolution. The convergence study of the tetrahedral grid is straightforward at a low solid volume fraction, $\alpha_s = 0.125$, achieved by configuring surface and volume mesh generation parameters to maintain a constant h^*. However, at maximum packing ($\alpha_s = \pi/6$), comparing its convergence with other methods using a common grid size becomes challenging, necessitating consideration of issues related to cell skewness.

A.2. Moderate-Reynolds-number flows

In contrast to the Stokes regime configuration, the effects of fluid inertia at moderate Reynolds numbers in the configuration of flows in ordered arrays of spheres are less studied [65,66], primarily due to the absence of an analytical solution. For instance, Hill et al. [65] approached $\alpha_s = 0.514 < \alpha_s^{max}$ and proposed a numerical correlation for $\mathcal{R}e \in [70, 160]$ using lattice-Boltzmann simulations. Up to the close-packed limits of arrays, only a few numerical methods are capable of accurately solving this problem within reasonable computational resources and time constraints (see Section 2.4).

In the configuration of close-packed cubic array of spheres, i.e. $\alpha_s = \alpha_s^{max} = \pi/6$, for various Reynolds numbers up to $\mathcal{R}e = 54$, we compare our numerical solutions provided by Code_Saturne on hybrid grids with highly accurate numerical solutions provided by the basilisk code on octree grids. Fig. A.4a shows very good agreement between the two numerical solutions with deviations inferior to 1.7% (the maximum

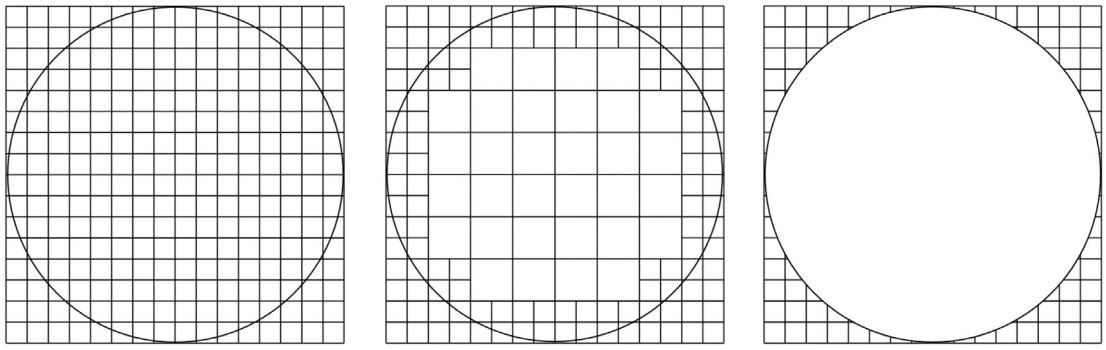

(a) uniform grid (b) octree grid (c) hybrid grid

Fig. A.1. 3D-mesh cross-section examples modeling a sphere in a tri-periodic cubic box: (a) Uniform grid with $N_{elts} = 16^3 = 4096$, (b) an example of octree grid with $N_{elts} = 3144$ demonstrating mesh refinement from $2^3 = 8$ to a maximum of $2^4 = 16$ points per dimension, and (c) hybrid grid with $N_{elts} = 2528$ composed of 1584 hexahedrons, 656 polyhedrons, 168 prisms and 120 tetrahedrons.

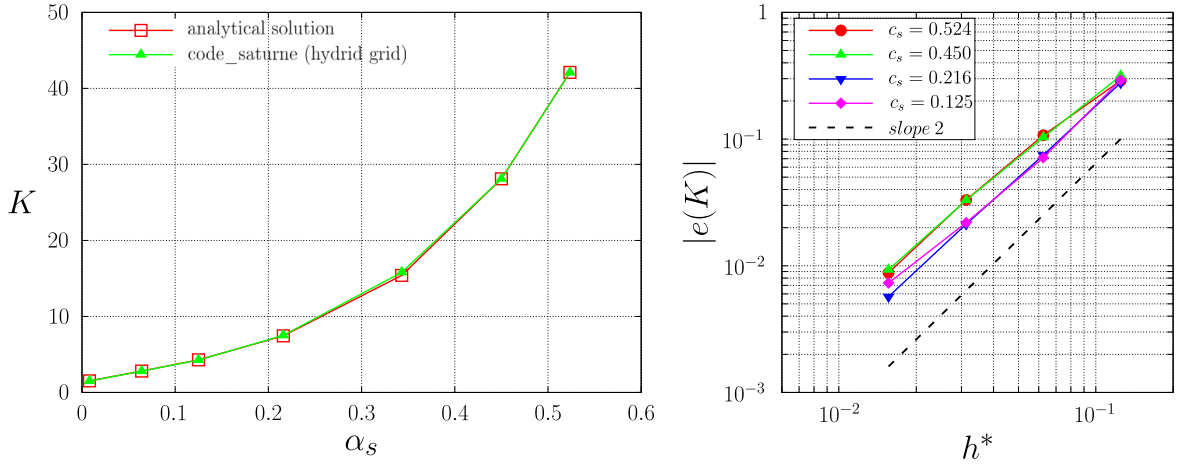

(a) (b)

Fig. A.2. Comparison of numerical results from Code_Saturne computed on a hybrid grid with the Zick and Homsy [13]'s analytical solution for the case of the flow through an infinite structured cubic-centered array of spheres at $Re = 0.01$: (a) Evolution of the friction coefficient K as a function of the solid volume fraction α_s, and (b) convergence of the K deviation as a function of the dimensionless grid size h^* for increasing solid volume fraction α_s.

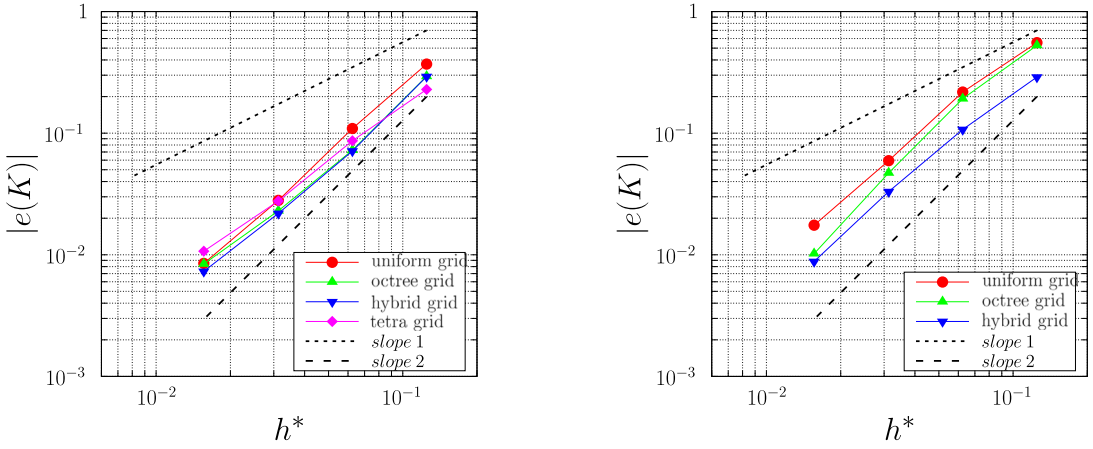

(a) $\alpha_s = 0.125$ (b) $\alpha_s = \pi/6$

Fig. A.3. Comparison of numerical results with the analytical solution of Zick and Homsy [13] for the case of Stokes flow through an infinite structured cubic-centered array of spheres at $Re = 0.01$. These results are computed using two different codes: basilisk with uniform and octree grids and Code_Saturne with hybrid and tetrahedral grids. The convergence of the computed solutions is plotted for two solid volume fractions (a) $\alpha_s = 0.125$ and (b) $\alpha_s = \pi/6$.

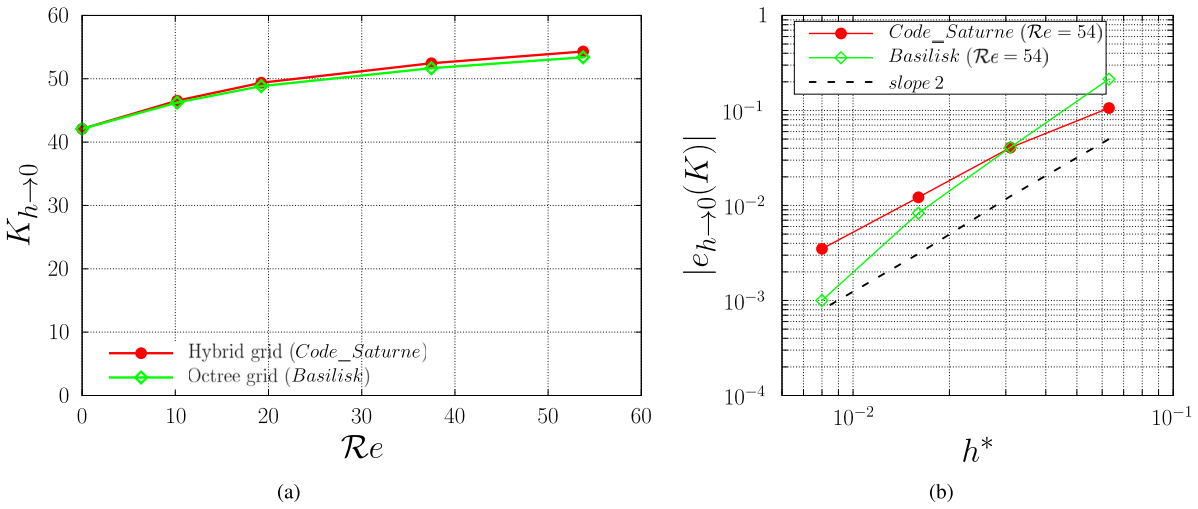

Fig. A.4. Comparison of numerical results from Code_Saturne computed on a hybrid grid and basilisk on a octree grid for the case of the flow through an infinite structured cubic-centered array of spheres: (a) Evolution of the extrapolated friction coefficient $K_{h\to 0}$ as a function of the Reynolds numbers $\mathcal{R}e$, and (b) convergence of the deviation $e_{h\to 0}(K)$ as a function of the dimensionless grid size h^* for $\mathcal{R}e = 54$.

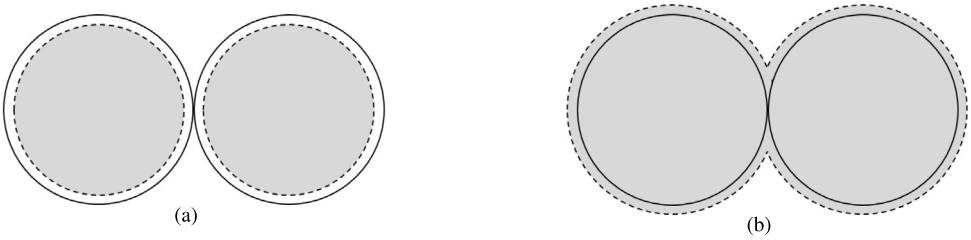

Fig. B.1. Schematic of two contact point modifications: (a) shrinking and (b) overlapping.

for $\mathcal{R}e = 54$). In Fig. A.4b, we compare their respective convergences with the same time step, $\Delta t = 5.10^{-3}$, and same Poisson and viscous solver tolerance, $tol = 10^{-7}$. Code_Saturne is 2nd-order accurate with a convergence rate $\alpha \sim 1.6$. In the basilisk case, the implemented advection scheme [26] is 2nd to 3rd-order accurate, inline with the computed rate $\alpha \sim 2.6$.

Appendix B. Contact point strategy

The study of contact points is a complex and central subject in flows through packed beds. The initial approaches involved shrinking the diameter of spherical particles (to 99% of their nominal diameter), as illustrated in Fig. B.1a to avoid contact and prevent cell skewness [27, 67]. Another approach suggested by Guardo et al. [68] involves enlarging sphere diameters to transform contact points into contact lines in 2D or contact surfaces in 3D, thereby reducing the skewness of cells in this area, as depicted in Fig. B.1b. However, modifying the particle sizes creates a subsequent deviation in the porosity and pressure drop values.

In this section, we employ the test case of flow through a periodic array of spheres, considering both Stokes and inertial regimes (as described in Section 3), to assess the deviation e of results generated from Code_Saturne. Table B.1 presents the deviations analysis of the numerical results for three shrinkage values, with a sphere diameter decreasing by 0.5%, 1% and 2%. The deviations between the reference solutions and our extrapolated solutions as h^* approaches zero are noted $e_{-2\%}$, $e_{-1\%}$ and $e_{-0.5\%}$. Additionally, for two enlargement values by increasing diameter sizes by 1% and 2%, the deviations are represented as $e_{+2\%}$ and $e_{+1\%}$.

The initial findings highlight slight discrepancies between the outcomes in the two selected regimes ($\mathcal{R}e = 0.01$ and $\mathcal{R}e = 54$). Besides, a $\pm 1\%$ modification of the diameter results in about 3% deviation of the solid volume fraction α_s. Examining the surface of an ideal sphere defined by a parametric equation, denoted as S_1 (details in Section 3.2), this modification generates an approximate deviation of $8\% - 9\%$ in the friction coefficient K, affecting the pressure drop and permeability similarly. For the surface, termed S_2, obtained from an ideal sphere after BSD processes (details in Section 3.3), the friction coefficient K deviation is approximately $7\% - 10\%$. These results are in line with the findings of Bai et al. [44] and confirm the "rule of thumb" identified by Dixon et al. [29], which suggests that a 1% increase in voidage corresponds to approximately a 3% increase in pressure drop error.

For a random array of spheres confined in a tube (low tube-to-particle ratio $D/d_p < 4$), Bai et al. [44] conducted coupled Discrete Element Method (DEM) and Computational Fluid Dynamics (CFD) simulations, demonstrating that particle shrinkage leads to similar conclusions. They presented empirical laws representing the evolution, in

Table B.1
Deviations e of the friction coefficient $K_{h\to 0}$ with the analytical solution $K_{ref} = 42.1$ for $\mathcal{R}e \ll 1$ and the numerical solution $K_{ref} = 54.3$ for $\mathcal{R}e = 54$, with variations in sphere diameter: decreasing by 0.5%, 1% and 2%, and increasing by 1% and 2%. The numerical results, obtained using Code_Saturne, for two different spherical surface processing techniques: the surface S_1 from an ideal sphere defined by a parametric equation and the surface S_2 from an ideal sphere after undergoing BSD processes.

Configurations	Regimes	Deviation e				
		$e_{-2\%}$	$e_{-1\%}$	$e_{-0.5\%}$	$e_{+1\%}$	$e_{+2\%}$
α_s	–	−0.059	−0.030	−0.015	0.030	0.059
$K_{h\to 0}$ (S_1)	$\mathcal{R}e \ll 1$	−0.155	−0.082	−0.042	0.094	0.195
	$\mathcal{R}e = 54$	−0.152	−0.079	−0.040	0.093	0.193
$K_{h\to 0}$ (S_2)	$\mathcal{R}e \ll 1$	−0.149	−0.074	−0.040	0.101	0.202
	$\mathcal{R}e = 54$	−0.148	−0.071	−0.039	0.101	0.194

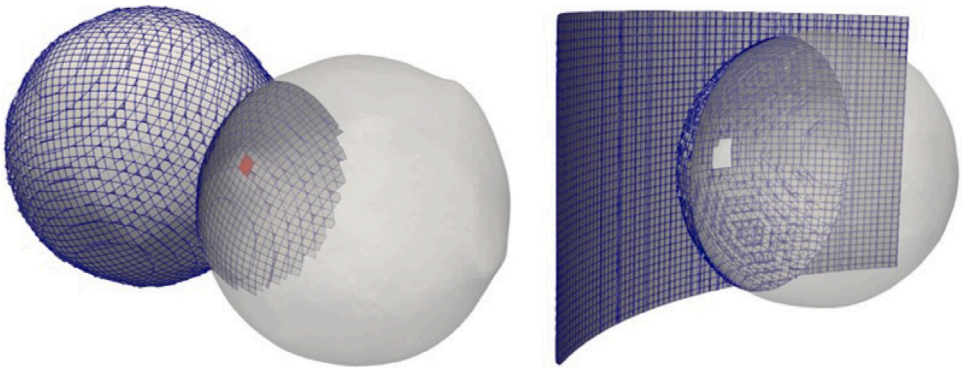

(a) Bead/Bead contact (b) Bead/Wall contact

Fig. B.2. Example of cell truncations in contact configurations: (a) for the Bead/Bead contact case: 4 mesh cells are truncated, represented with a red square, and (b) for the Bead/Wall contact case with 15 truncated mesh cells, represented in white.

percentage, of pressure drop deviation ($\varepsilon_{\Delta p}$) as a function of porosity deviation (ε_{α_f}) such as:

$$\varepsilon_{\Delta p} = 3.385\varepsilon_{\alpha_f} - 0.045\varepsilon_{\alpha_f}^2 \tag{B.1}$$

In the case of 3D digital rock reconstruction, controlling porosity requires a delicate balance in discretization. It should be fine enough to achieve numerical convergence and accurate enough to preserve geometric boundaries, all while remaining coarse enough to manage computational costs. Unlike ideal spheres, there is no need for bead shrinkage or enlargement methods. The segmentation and geometric modeling processes naturally flatten glass bead shapes locally near contact points, as depicted in Figs. 2(d) and 2(e). Methods proposed by Eppinger et al. [69] and Dixon et al. [29] address local flattening on spheres by removing spherical caps at contact points, demonstrating a significantly lower impact on porosity and pressure drop compared to sphere shrinkage or enlargement methods.

Depending on the mesh resolution, there are configurations where the mesh size h is significantly larger than the voxel size h_{vox} near contact points. To avoid skewness in cells in the proximity of these regions and to guarantee mesh quality, the meshing algorithm is allowed to skip these cells. Examples of cell truncations are illustrated in Fig. B.2a for the Bead/Bead contact case, and in Fig. B.2b for the Bead/Wall contact case. Particular attention is given to mesh joinings between concave (wall tube) and convex (beads) surfaces, which generate larger contact surfaces than convex/convex mesh joinings.

References

[1] Larachi F, Hannaoui R, Horgue P, Augier F, Haroun Y, Youssef S, Rosenberg E, Prat M, Quintard M. X-ray micro-tomography and pore network modeling of single-phase fixed-bed reactors. Chem Eng J 2014;240:290–306. http://dx.doi.org/10.1016/j.cej.2013.11.077.

[2] Soulaine C, Gjetvaj F, C. G, Roman S, Russian A, Gouze P, H.A. T. The impact of sub-resolution porosity of X-ray microtomography images on the permeability. Transp Porous Media 2016;113:227–43. http://dx.doi.org/10.1007/s11242-016-0690-2.

[3] Bultreys T, De Boever W, Cnudde V. Imaging and image-based fluid transport modeling at the pore scale in geological materials: A practical introduction to the current state-of-the-art. Earth-Sci Rev 2016;155:93–128. http://dx.doi.org/10.1016/j.earscirev.2016.02.001.

[4] Kelly S, El-Sobky H, Torres-Verdín C, Balhoff MT. Assessing the utility of FIB-SEM images for shale digital rock physics. Adv Water Resour 2016;95:302–16. http://dx.doi.org/10.1016/j.advwatres.2015.06.010, Pore scale modeling and experiments.

[5] Larmagnat S, Des Roches M, Daigle L, Francus P, D. L, Raymond J, Malo M, Aubiès-Trouilhc A. Continuous porosity characterization: Metric-scale intervals in heterogeneous sedimentary rocks using medical CT-scanner. Mar Pet Geol 2019;109:361–80. http://dx.doi.org/10.1016/j.marpetgeo.2019.04.039.

[6] Orlov D, Ebadi M, Muravleva E, Volkhonskiy D, Erofeev A, Savenkov E, Balashov V, Belozerov B, Krutko V, Yakimchuk I, Evseev N, Koroteev D. Different methods of permeability calculation in digital twins of tight sandstones. J Nat Gas Sci Eng 2021;87:103750. http://dx.doi.org/10.1016/j.jngse.2020.103750.

[7] Baldo CR, Probst GM, Dewulf W. Performance evaluation of an image-based measurement method used to determine the geometric errors of cone-beam CT instruments. Adv Ind Manuf Eng 2020;1:100004. http://dx.doi.org/10.1016/j.aime.2020.100004.

[8] Hammouti A, Larmagnat S, Rivard C, Pham Van Bang D. Use of CT-scan images to build geomaterial 3D pore network representation in preparation for numerical simulations of fluid flow and heat transfer, Quebec. Geological Survey of Canada; 2023, p. 49. http://dx.doi.org/10.4095/331502, Open file 8954.

[9] Andrä H, Combaret N, Dvorkin J, Glatt E, Han J, Kabel M, Keehm Y, Krzikalla F, Lee M, Madonna C, Marsh M, Mukerji T, Saenger EH, Sain R, Saxena N, Ricker S, Wiegmann A, Zhan X. Digital rock physics benchmarks. Part I: Imaging and segmentation. Comput Geosci 2013a;50:25–32. http://dx.doi.org/10.1016/j.cageo.2012.09.005.

[10] Andrä H, Combaret N, Dvorkin J, Glatt E, Han J, Kabel M, Keehm Y, Krzikalla F, Lee M, Madonna C, Marsh M, Mukerji T, Saenger EH, Sain R, Saxena N, Ricker S, Wiegmann A, Zhan X. Digital rock physics benchmarks. Part II: Computing effective properties. Comput Geosci 2013b;50:33–43. http://dx.doi.org/10.1016/j.cageo.2012.09.008.

[11] Kerimov A, Mavko G, Mukerji T, Dvorkin J, Al Ibrahim MA. The influence of convex particles' irregular shape and varying size on porosity, permeability, and elastic bulk modulus of granular porous media: Insights from numerical simulations. J Geophys Res: Solid Earth 2018;123(12):10,563–82. http://dx.doi.org/10.1029/2018JB016031.

[12] Hasimoto H. On the periodic fundamental solutions of the Stokes equations and their application to viscous flow past a cubic array of spheres. J Fluid Mech 1959;5:317–28. http://dx.doi.org/10.1017/S0022112059000222.

[13] Zick A, Homsy G. Stokes flow through periodic arrays of spheres. J Fluid Mech 1982;115(1):13–26. http://dx.doi.org/10.1017/s0022112082000627.

[14] Ergun S. Fluid flow through packed columns. Chem Eng Prog 1952;48:89–94.

[15] Reichelt W. Zur berechnung des druckverlustes einphasigdurchstrokmter kugel- und zylinderschukttungen. Chem Ing Tech 1972;44:1068–71. http://dx.doi.org/10.1002/cite.330441806.

[16] Van Der Hoef MA, Beetstra R, Kuipers JAM. Lattice-Boltzmann simulations of low-Reynolds-number flow past mono- and bidisperse arrays of spheres: results for the permeability and drag force. J Fluid Mech 2005;528:233–54. http://dx.doi.org/10.1017/S0022112004003295.

[17] Wachs A, Hammouti A, Vinay G, Rahmani M. Accuracy of finite volume/staggered grid distributed Lagrange multiplier/fictitious domain simulations of particulate flows. Comput & Fluids 2015;115:154–72. http://dx.doi.org/10.1016/j.compfluid.2015.04.006.

[18] Chen S, Doolen GD. Lattice Boltzmann method for fluid flows. Annu Rev Fluid Mech 1998;30(1):329–64. http://dx.doi.org/10.1146/annurev.fluid.30.1.329.

[19] Keehm Y. Computational rock physics: Transport properties in porous media and applications (Ph.D. Dissertation), Stanford University; 2003, p. 135.

[20] Peskin C. The immersed boundary method. Acta Numer 2002;11(1):479–517. http://dx.doi.org/10.1017/S0962492902000077.

[21] Tenneti S, Garg R, Subramaniam S. Drag law for monodisperse gas-solid systems using particle-resolved direct numerical simulation of flow past fixed assemblies of spheres. Int J Multiph Flow 2011;37(9):1072–92. http://dx.doi.org/10.1016/j.ijmultiphaseflow.2011.05.010.

[22] Glowinski R, Pan T-W, Hesla T, Joseph D. A distributed Lagrange multiplier/fictitious domain method for particulate flows. Int J Multiph Flow 1999;25(5):755–94. http://dx.doi.org/10.1016/S0301-9322(98)00048-2.

[23] Aidun CK, Clausen JR. Lattice-Boltzmann method for complex flows. Annu Rev Fluid Mech 2010;42(1):439–72. http://dx.doi.org/10.1146/annurev-fluid-121108-145519.

[24] Hammouti A, Lemaitre A. A second-order pressure-accurate finite-difference scheme for the Stokes problem with rigid non-conforming boundaries. 2011, p. 1–13, arXiv:1110.1311.

[25] Roma AM, Peskin CS, Berger MJ. An adaptive version of the immersed boundary method. J Comput Phys 1999;153(2):509–34. http://dx.doi.org/10.1006/jcph.1999.6293.

[26] Chowdhury R. Higher-order adaptive methods for fluid dynamics (Ph.D. Dissertation), Sorbonne University; 2019, p. 111.

[27] Dixon A, Nijemeisland M. CFD as a design tool for fixed-bed reactors. Ind Eng Chem Res 2001;40:5246–54. http://dx.doi.org/10.1021/ie001035a.

[28] Moghaddam E, Foumeny E, Stankiewicz A, Padding J. Fixed bed reactors of non-spherical pellets: Importance of heterogeneities and inadequacy of azimuthal averaging. Chem Eng Sci: X 2019;1:100006. http://dx.doi.org/10.1016/j.cesx.2019.100006.

[29] Dixon A, Nijemeisland M, Stitt E. Systematic mesh development for 3D CFD simulation of fixed beds: Contact points study. Comput Chem Eng 2013;48:135–53. http://dx.doi.org/10.1016/j.compchemeng.2012.08.011.

[30] Arenhart FA, Nardelli VC, Donatelli GD. Comparison of surface-based and image-based quality metrics for the analysis of dimensional computed tomography data. Case Stud Nondestruct Test Eval 2016;6:111–21. http://dx.doi.org/10.1016/j.csndt.2016.05.002, Special Issue: Industrial computed tomography.

[31] Pontana F, Pagniez J, Flohr T, Faivre J-B, Duhamel A, Remy J, Remy-Jardin M. Chest computed tomography using iterative reconstruction vs filtered back projection (Part 1): evaluation of image noise reduction in 32 patients. Eur Radiol 2011;21:627–35. http://dx.doi.org/10.1007/s00330-010-1990-5.

[32] Vardhanabhuti V, Loader RJ, Mitchell GR, Riordan1 RD, Roobottom CA. Image quality assessment of standard- and low-dose chest CT using filtered back projection, adaptive statistical iterative reconstruction, and novel model-based iterative reconstruction algorithms. Am J Roentgenol 2013;200:545–62. http://dx.doi.org/10.2214/ajr.12.9424.

[33] Beister M, Kolditz D, Kalender WA. Iterative reconstruction methods in X-ray CT. Phys Medica 2012;28:94–108. http://dx.doi.org/10.1016/j.ejmp.2012.01.003.

[34] Kruth J, Bartscher M, Carmignato S, Schmitt R, De Chiffre L, Weckenmann A. Computed tomography for dimensional metrology. CIRP Ann 2011;60(2):821–42. http://dx.doi.org/10.1016/j.cirp.2011.05.006.

[35] Andó E, Marks B, Roux S. Single-projection reconstruction technique for positioning monodisperse spheres in 3D with a divergent x-ray beam. Meas Sci Technol 2021;32:095405. http://dx.doi.org/10.1088/1361-6501/abfbfe.

[36] Otsu N. A threshold selection method from gray-level histograms. IEEE Trans Syst Man Cybern 1979;9:62–6. http://dx.doi.org/10.1109/TSMC.1979.4310076.

[37] Meyer F. Topographic distance and watershed lines. Signal Process 1994;38:113–25. http://dx.doi.org/10.1016/0165-1684(94)90060-4.

[38] Sendov B. Hausdorff distance and image processing. Russian Math Surveys 2004;59(2):319–28. http://dx.doi.org/10.1070/RM2004v059n02ABEH000721.

[39] Karimi D, Salcudean S. Reducing the hausdorff distance in medical image segmentation with convolutional neural networks. IEEE Trans Med Imaging 2019;32(2):499–513. http://dx.doi.org/10.1109/TMI.2019.2930068.

[40] Cignoni P, Rocchini C, Scopigno R. Metro: measuring error on simplified surfaces. In: Computer graphics forum. Vol. 17, Blackwell Publishers; 1998, p. 167–74.

[41] Hammouti A. Simulation numérique directe en différence finie de l'écoulement d'un fluide incompressible en présence d'interfaces rigides (Ph.D. Dissertation), France: École des Ponts et Chaussées; 2009, p. 214.

[42] Guibert R, Nazarova M, Horgue P, Hamon G, Creux P, Debenest G. Computational permeability determination from pore-scale Imaging: Sample size, mesh and method Sensitivities. Transp Porous Media 2015;103(3):641–56. http://dx.doi.org/10.1007/s11242-015-0458-0.

[43] Ribes A, Caremoli C. Salome platform component model for numerical simulation. In: 31st annual international computer software and applications conference. COMPSAC 2007, Vol. 2, 2007, p. 553–64. http://dx.doi.org/10.1109/COMPSAC.2007.185.

[44] Bai H, Theuerkauf J, Gillis PA, Witt PM. A coupled DEM and CFD simulation of flow field and pressure drop in fixed bed reactor with randomly packed catalyst particles. Ind Eng Chem Res 2009;48(8):4060–74. http://dx.doi.org/10.1021/ie801548h.

[45] Archambeau F, Méchitoua N, Sakiz M. Code Saturne: A finite volume code for the computation of turbulent incompressible flows - Industrial applications. Int J Finite Vol 2004;1–63, URL: http://api.semanticscholar.org/CorpusID:125105489.

[46] Richardson LF, Glazebrook RT. IX. The approximate arithmetical solution by finite differences of physical problems involving differential equations, with an application to the stresses in a masonry dam. Phil Trans R Soc A 1911;210(459–470):307–57. http://dx.doi.org/10.1098/rsta.1911.0009.

[47] Gerke KM, Vasilyev RV, Khirevich S, Collins D, Karsanina MV, Sizonenko TO, Korost DV, Lamontagne S, Mallants D. Finite-difference method Stokes solver (FDMSS) for 3D pore geometries: Software development, validation and case studies. Comput Geosci 2018;114:41–58. http://dx.doi.org/10.1016/j.cageo.2018.01.005.

[48] Lesueur M, Rattez H, Colomes O. μCT scans permeability computation with an unfitted boundary method to improve coarsening accuracy. Comput Geosci 2022;166:105–18. http://dx.doi.org/10.1016/j.cageo.2022.105118.

[49] Saff E, Kuijlaars A. Distributing many points on a sphere. Math Intelligencer 1997;19:5–11. http://dx.doi.org/10.1007/BF03024331.

[50] Uhlmann M. An immersed boundary method with direct forcing for the simulation of particulate flows. J Comput Phys 2005;209(2):448–76. http://dx.doi.org/10.1016/j.jcp.2005.03.017.

[51] Dahlberg BEJ. On the distribution of Fekete points. Duke Math J 1978;45(3):537–42. http://dx.doi.org/10.1215/S0012-7094-78-04524-6.

[52] Bernardini F, Mittleman J, Rushmeier HE, Silva CT, Taubin G. The ball-pivoting algorithm for surface reconstruction. IEEE Trans Vis Comput Graphics 1999;5:349–59. http://dx.doi.org/10.1109/2945.8173513.

[53] Bernard D. 3D quantification of pore scale geometrical changes using synchrotron computed. Oil Gas Sci Technol-Rev Inst Fr Pet 2005;60:747–62, URL: http://dx.doi.org/10.2516/OGST:2005053.

[54] Ahrens J, Geveci B, Law C. ParaView: An end-user tool for large data visualization. In: Visualization handbook. Elsevier; 2005, p. 717–31.

[55] Cignoni P, Callieri M, Corsini M, Dellepiane M, Ganovelli F, Ranzuglia G. MeshLab: an open-source mesh processing tool. In: Scarano V, Chiara RD, Erra U, editors. Eurographics Italian chapter conference. The Eurographics Association; 2008, p. 129–36. http://dx.doi.org/10.2312/LocalChapterEvents/ItalChap/ItalianChapConf2008/129-136.

[56] Euzenat F, Hammouti A, Climent E, Fede P, Wachs A. Effect of spatial filter features on local heat transfer coefficients obtained from particle-resolved simulations of a flow through a fixed random array of rigid spherical particles. Int J Heat Fluid Flow 2021;92:108873. http://dx.doi.org/10.1016/j.ijheatfluidflow.2021.108873.

[57] Hammouti A, Euzenat F, Rakotonirina A, Rolland M, Wachs A. Direct numerical simulation of reactive flow through fixed bed of catalyst particles. In: Proc. of sixth int. conf. on porous media and its appl. in sc., eng. and ind. ECI symposium series. 2016, p. 1–6.

[58] Sulaiman M, Climent E, Wachs A, Hammouti A. Numerical simulations and modelling of mass transfer through random assemblies of catalyst particles: From dilute to dense reactive particulate regime. Chem Eng Sci 2020;223:115659. http://dx.doi.org/10.1016/j.ces.2020.115659.

[59] Fedkiw R, Aslam T, Merriman B, Osher S. A non-oscillatory Eulerian approach to interfaces in multimaterial flows (the ghost fluid method). J Comput Phys 1999;152(2):457–92. http://dx.doi.org/10.1006/jcph.1999.6236.

[60] Griffith BE, Peskin CS. On the order of accuracy of the immersed boundary method: Higher order convergence rates for sufficiently smooth problems. J Comput Phys 2005;208(1):75–105. http://dx.doi.org/10.1016/j.jcp.2005.02.011.

[61] Wachs A. Particle-scale computational approaches to model dry and saturated granular flows of non-Brownian, non-cohesive, and non-spherical rigid bodies. Acta Mech 2019;230:1919–80. http://dx.doi.org/10.1007/s00707-019-02389-9.

[62] Morente A, Goyal A, Wachs A. A highly scalable direction-splitting solver on regular Cartesian grid to compute flows in complex geometries described by STL files. Fluids 2023;8(3). http://dx.doi.org/10.3390/fluids8030086.

[63] Deen N, Kriebitzsch S, van der Hoef M, Kuipers J. Direct numerical simulation of flow and heat transfer in dense fluid-particle systems. Chem Eng Sci 2012;88:329–44. http://dx.doi.org/10.1016/j.ces.2012.06.055.

[64] Popinet S. A quadtree-adaptive multigrid solver for the Serre-Green-Naghdi equations. J Comput Phys 2015;302:336–58. http://dx.doi.org/10.1016/j.jcp.2015.09.009.

[65] Hill R, Koch D, Ladd J. Moderate Reynolds number flows in ordered and random arrays ofarrays of spheres. J Fluid Mech 2001;448:243–78.

[66] Beetstra R, van der Hoef MA, Kuipers JAM. Drag force of intermediate Reynolds number flow past mono- and bidisperse arrays of spheres. AIChE J 2007;53(2):489–501. http://dx.doi.org/10.1002/aic.11065.

[67] Calis H, Nijenhuis J, Paikert B, Dautzenberg F, van den Bleek C. CFD modelling and experimental validation of pressure drop and flow profile in a novel structured catalytic reactor packing. Chem Eng Sci 2001;56(4):1713–20. http://dx.doi.org/10.1016/S0009-2509(00)00400-0.

[68] Guardo A, Coussirat M, Larrayoz M, Recasens F, Egusquiza E. CFD flow and heat transfer in nonregular packings for fixed bed equipment design. Transp Porous Media 2001;43(22):7049–56. http://dx.doi.org/10.1021/ie034229+.

[69] Eppinger T, Seidler K, Kraume M. DEM-CFD simulations of fixed bed reactors with small tube to particle diameter ratios. Chem Eng J 2011;166(1):324–31. http://dx.doi.org/10.1016/j.cej.2010.10.053.